



Structure of the Synthetic K-rich Phyllomanganate Birnessite Obtained by High-Temperature Decomposition of KMnO_4 . Substructures of K-rich Birnessite from 1000C Experiment

Anne-Claire Gaillot, Victor A. Drits, Alain Manceau, Bruno Lanson

► To cite this version:

Anne-Claire Gaillot, Victor A. Drits, Alain Manceau, Bruno Lanson. Structure of the Synthetic K-rich Phyllomanganate Birnessite Obtained by High-Temperature Decomposition of KMnO_4 . Substructures of K-rich Birnessite from 1000C Experiment. *Microporous and Mesoporous Materials*, Elsevier, 2007, 98, pp.267-282. <10.1016/j.micromeso.2006.09.010>. <hal-00193628>

HAL Id: hal-00193628

<https://hal.archives-ouvertes.fr/hal-00193628>

Submitted on 4 Dec 2007

HAL is a multi-disciplinary open access archive for the deposit and dissemination of scientific research documents, whether they are published or not. The documents may come from teaching and research institutions in France or abroad, or from public or private research centers.

L'archive ouverte pluridisciplinaire **HAL**, est destinée au dépôt et à la diffusion de documents scientifiques de niveau recherche, publiés ou non, émanant des établissements d'enseignement et de recherche français ou étrangers, des laboratoires publics ou privés.

1 **Structure of the Synthetic K-rich Phylломanganate Birnessite Obtained**
2 **by High-Temperature Decomposition of KMnO₄.**

3 **Substructures of K-rich Birnessite from 1000°C Experiment.**

4
5
6 **Anne-Claire Gaillot¹**

7 **Victor A. Drits^{1,2}**

8 **Alain Manceau¹**

9 **Bruno Lanson^{1,*}**

10
11 1 – Environmental Geochemistry Group, LGIT-Maison des Géosciences, University of
12 Grenoble - CNRS, 38041 Grenoble Cedex 9, France.

13 2 – Geological Institute, Russian Academy of Sciences, 7 Pyzhevsky street, 109017 Moscow,
14 Russia

15
16 * Author to whom correspondence should be addressed.

17 e-mail: bruno.lanson@obs.ujf-grenoble.fr, Tel.: +33 476 828 017, Fax: +33 476 828 101

Abstract

18

19

20 The structure of a synthetic potassium-rich birnessite prepared from the thermal
21 decomposition of KMnO_4 at 1000°C in air has been refined by Rietveld analysis of the
22 powder X-ray diffraction (XRD) data, and the structure model shown to be consistent with
23 extended X-ray absorption fine structure data. K-rich birnessite structure is a two-layer
24 orthorhombic polytype ($2O$) with unit-cell parameters $a = 5.1554(3) \text{ \AA}$, $b = 2.8460(1) \text{ \AA}$, $c =$
25 $14.088(1) \text{ \AA}$, $\alpha = \beta = \gamma = 90^\circ$, $a/b = \sqrt{3.281}$, and was refined in the $Ccmm$ space group. The
26 structure is characterized by the regular alternation of octahedral layers rotated with respect to
27 each other by 180° . Octahedral layers are essentially devoid of vacant sites, the presence of
28 $0.25 \text{ Mn}^{3+}_{\text{layer}}$ cations within these layers being the main source of their deficit of charge,
29 which is compensated for by interlayer K^+ cations. Mn^{3+} octahedra, which are distorted by the
30 Jahn-Teller effect, are systematically elongated along the **a** axis (cooperative Jahn-Teller
31 effect) to minimize steric strains, thus yielding an orthogonal layer symmetry. In addition,
32 Mn^{3+} octahedra are segregated in Mn^{3+} -rich rows parallel to the **b** axis that alternate with two
33 Mn^{4+} rows according to the sequence $\dots\text{-Mn}^{3+}\text{-Mn}^{4+}\text{-Mn}^{4+}\text{-Mn}^{3+}\text{-}\dots$ along the **a** direction,
34 thus leading to a $\mathbf{A} = 3\mathbf{a}$ super-periodicity. At 350°C , the structure partially collapses due to
35 the departure of interlayer H_2O molecules and undergoes a reversible $2O$ -to- $2H$ phase
36 transition. This transition results from the relaxation of the cooperative Jahn-Teller effect, that
37 is from the random orientation of elongated Mn^{3+} octahedra.

Introduction

38
39
40
41
42
43
44
45
46
47
48
49
50
51
52
53
54
55
56
57
58
59
60
61
62
63

Birnessite is a phylломanganate, that is a manganese oxide containing predominantly Mn^{4+} cations assembled in layers of edge-sharing MnO_6 octahedra. A layer charge deficit arises from the presence within layers of Mn^{3+} cations and/or vacant layer octahedra and is compensated for by the presence of interlayer cations which are typically hydrolysable cations [1-8]. As such phylломanganates are very similar to expandable 2:1 phyllosilicates (smectites) and can be considered as $(2 \times \infty)$ microporous solids [9,10]. As smectites, phylломanganates can be intercalated with a variety of organic and inorganic compounds to form multilayer nanocomposites [11-17], or pillared structures [18-24]. In addition, phylломanganates have been widely used as templates for the formation of octahedral molecular sieves with variable tunnel sizes that have demonstrated excellent potential in heterogeneous catalysis, hazardous waste remediation, and rechargeable battery technology [25-42]. More recently, mesoporous hollow shells with birnessite walls have also been synthesized [43].

Besides, birnessites play a pivotal role in the fate of heavy metals and other pollutants in contaminated water systems and soils because they possess unique crystal-chemical characteristics which confer them extensive redox and sorption properties [3,6,44-49]. A large range of birnessite varieties with different structural and chemical characteristics can be synthesized in the laboratory. Synthetic birnessite can be obtained from the oxidation of Mn^{2+} in highly alkaline medium [1,2,50,51], from the thermal decomposition of MnO-containing mixtures [52], and from the reduction of Mn^{7+} [53-59]. In most cases, syntheses are performed at low temperature to obtain surrogate materials representative of natural specimens [1,2,60,61]. Low-temperature birnessites are usually finely dispersed, and often present a low degree of structural order.

Over the last decade an interest for high temperature birnessite (from 170°C up to 1000°C) has emerged as the result of their promising potential as electrodes in secondary

64 lithium batteries [52,56-58,62-65]. Kim et al. showed that birnessites with high structural
65 perfection can be obtained at high temperature, these varieties being more stable than those
66 commonly used in electrochemistry [58]. In particular the transition to a spinel structure was
67 not observed after cell cycling. The protocol is based on the thermal decomposition of
68 KMnO_4 , large K^+ cations pillaring the synthesis products, thus stabilizing the layered
69 framework. In addition, the production of highly oxidizing species during the decomposition
70 prevents the formation of suboxides. As a result, a new variety of synthetic K-rich birnessites
71 with a two-layer periodicity along the c axis was obtained [58]. This variety will be hereafter
72 referred to as KBi. These authors performed experiments from 200-1000°C, but structural and
73 crystal chemical study was limited to high-temperature varieties. The Rietveld technique was
74 used to determine the crystal structure of KBi obtained at 800°C. In the refined model
75 adjacent vacancy-free layers are rotated with respect to each other by 180° around the c axis,
76 which is perpendicular to the layers, and interlayer K^+ is located in a prism defined by
77 tridentate cavities of adjacent layers [58]. Kim et al. also synthesized at 1000°C a KBi sample
78 that presents a different chemistry but did not refine its structure [58].

79 The present article, together with its companion [66], further extends the structural
80 characterization of high-temperature KBi synthesized according to the protocol of Kim et al.
81 [58]. This series of articles was initiated by the structure refinement of a KBi sample obtained
82 at 800°C from single-crystal and powder X-ray diffraction (XRD) and extended X-ray
83 absorption fine structure (EXAFS) spectroscopy experiments [67]. XRD structure refinement
84 has pointed out several significant differences with the model proposed by Kim et al. [58,67].
85 First, the cation composition of KBi interlayers is heterogeneous and includes both K^+ and
86 Mn^{3+} cations. Second, layers of KBi synthesized at 800°C contain significant amount of
87 vacant octahedra (12%) and consist exclusively of Mn^{4+} octahedra because of the layer-to-
88 interlayer migration of Mn^{3+} cations. Third, interlayer K^+ is not located in the prism's center
89 but its site is split into three ones, each of which is shifted toward the nearest prism's face in

90 the interlayer mid plane. The determination of these fine structure details should provide a
91 better understanding of the relationship between KBi structure and its properties. The second
92 paper of this series describes the phase and structural heterogeneities of KBi samples
93 synthesized at 200-1000°C, together with the factors responsible for these heterogeneities
94 [68]. The present work is devoted to the structural characterization of a homogeneous KBi
95 sample obtained at 1000°C and of this KBi variety when heated to 350°C. The present article
96 will focus on the average distribution of layer and interlayer cations within the subcell and on
97 the origin of the layer charge, whereas KBi superstructure and its origin will be discussed in
98 the last part of this series of articles devoted to high-temperature KBi structure [66]. One
99 effective tool to study superstructures is to use, along with XRD, selected area electron
100 diffraction (SAED) [5,6,46,69-71]. However, comparison of XRD and SAED data may
101 appear irrelevant because of the possible modification of interlayer species distribution as the
102 result of dehydration under vacuum [57]. XRD experiments were thus performed under deep
103 vacuum conditions to check the consequences of such dehydration on the layer structure and
104 on the interlayer cation distribution.

105

106

Experimental Section

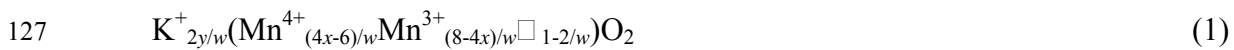
107

108 **Experimental Methods.** K-rich phyllosmanganate birnessite (hereafter referred to as
109 KBi) was prepared by thermal decomposition of fine grained KMnO_4 powder (particle size <
110 $50\ \mu\text{m}$) at 1000°C in air according to the procedure of Kim et al. [58,67]. As for the 800°C
111 synthesis, structural homogeneity of synthetic products was maximized by using flat crucibles
112 containing a thin layer of KMnO_4 powder. KBi samples synthesized at 1000°C (this study)
113 and 800°C will be hereafter referred to as KBi_{10} and KBi_8 [67], respectively.

114 The morphology of KBi_{10} particles was observed on a JEOL JSM 6320F high-resolution
115 scanning electron microscope equipped with a field emission electron source. No significant

116 difference in size or shape was observed between KBi_8 and KBi_{10} crystals, and KBi_{10} particles
117 consist of large micro-crystals with well-defined crystallographic faces [67].

118 **Thermal and Chemical Analyses.** Thermal analyses were carried out with a NETZSCH
119 Simultan STA 409 EP analyzer. DT-TG data were recorded in air using a $6^\circ\text{C}/\text{min}$ heating
120 rate over the $20\text{-}1100^\circ\text{C}$ temperature range to determine the amount of structural water. Total
121 K and Mn contents were determined using a Perkin-Elmer Optima 3000 ICP-AES after
122 digestion of about 8 mg of KBi powder in 200 mL of 1% HNO_3 / 0.1% NH_3OHCl matrix.
123 The mean oxidation degree of manganese in birnessite was determined by potentiometric
124 titration using $(\text{NH}_4)_2\text{Fe}(\text{SO}_4)$ Mohr salt and $\text{Na}_4\text{P}_2\text{O}_7$ [72,73]. The mean oxidation state, $2x$,
125 in combination with the atomic ratio $y = \text{K}/\text{Mn}$ determined from the chemical analyses, allows
126 calculating the structural formula of KBi using the relation [67]:



128 where $w = \frac{2x + y}{2}$ and \square represents vacant layer sites. This structural formula can be refined
129 by taking into account the amount of interlayer H_2O molecules ($\text{H}_2\text{O}_{\text{interlayer}}$) deduced from the
130 DT-TG curves.

131 **X-Ray Diffraction Data Collection.** Powder XRD patterns were recorded using a
132 Bruker D5000 powder diffractometer equipped with a Kevex Si(Li) solid detector and
133 $\text{CuK}\alpha_{1+2}$ radiation. Intensities were recorded from 5 to 90° with a 0.04° 2θ interval, using a
134 40 sec counting time per step. A rotating sample holder was used for room temperature
135 measurements to minimize the effect of preferential orientation. A Anton Paar TTK450
136 chamber was used to record XRD patterns from samples heated *in situ*. XRD patterns of
137 KBi_{10} obtained at 100°C , 150°C , 250°C and 350°C will be hereafter referred to as 100- KBi_{10} ,
138 150- KBi_{10} , 250- KBi_{10} and 350- KBi_{10} , respectively, while the notations KBi_{10} and AfterT-
139 KBi_{10} will be used to differentiate XRD patterns recorded at room-temperature before and
140 after temperature experiments, respectively. All heated KBi diffractograms were recorded
141 successively in a single experiment. The sample was heated *in situ* at a $6^\circ\text{C}/\text{min}$ rate until the

142 target temperature was reached and maintained at a temperature plateau for two hours before
143 collecting the diffractogram using the same conditions than at room temperature. After ~24
144 hours of data collection, temperature was further increased to the next two-hour plateau. XRD
145 data was finally collected again after cooling the sample back to room temperature (sample
146 AfterT-KBi₁₀). Finally, the same Anton Paar TTK450 chamber allowed studying the structure
147 of KBi₁₀ under deep vacuum conditions using a Varian V70 turbo-molecular pump connected
148 to the sample chamber to reach $\sim 10^{-5}$ hPa. After waiting for 15 hours to ensure a complete
149 dehydration of the sample, XRD data was collected using the same experimental conditions.
150 This sample will be referred to as Vacuum-KBi₁₀, while the XRD pattern recorded once back
151 at the atmospheric pressure to allow rehydration of this sample will be referred to as
152 AfterVac-KBi₁₀. Note that indexing was performed systematically assuming an orthorhombic
153 C-centered unit cell whatever the actual layer symmetry (orthogonal or hexagonal).

154 **Simulation of Powder XRD Patterns.** The Rietveld technique was used to refine the
155 structure of sample KBi₁₀ using the XND code [74]. To de-correlate instrumental broadening,
156 profile shape function (PSF) parameters and spectral distribution were refined first using a
157 reference quartz powder sample [8]. During the subsequent structure refinement process these
158 instrumental parameters were not further refined. A spline function was used to interpolate a
159 background defined by 6-to-8 points. Scale factor and unit-cell parameters were refined first
160 before site coordinates and occupancies. Atomic thermal motion was modeled using isotropic
161 Debye-Waller factors (B). In the final stage of the refinement, orientation parameters were
162 introduced using first degree spherical functions. Fit quality was estimated with the standard
163 R_{wp} and R_B factors. More details on the XND code can be found at
164 <http://www.ccp14.ac.uk/ccp/ccp14/ftp-mirror/xnd/pub/xnd/html/xnd.html>.

165 **EXAFS Experiments.** Mn EXAFS spectra were recorded at the LURE synchrotron
166 radiation laboratory (Orsay – France) on the D42 spectrometer of the EXAFS I station.
167 Experimental conditions and data analysis were the same as those reported for KBi₈ [67]. The

168 EXAFS spectra were apodized by a Kaiser-Bessel function ($\beta = 2.5$) and then Fourier
169 transformed to real space to generate radial structure functions (RSFs). RSFs were not
170 corrected for phase shifts, causing peaks to appear at shorter distances ($R + \Delta$, with $\Delta \approx -$
171 0.4 \AA) relative to the true interatomic distances (R). Structural parameters from the nearest
172 oxygen and manganese shells (Mn-O and Mn-Mn atomic pairs) were determined by back-
173 transforming to k space the first two RSF peaks, and fitting the data with phase shift and
174 amplitude functions calculated by FEFF7 using λ -MnO₂ as structure model [75,76]. The
175 short-distance Mn-O and Mn-Mn contributions were fitted together because of incomplete
176 separation in the Fourier-filtering process.

177

178 **Results**

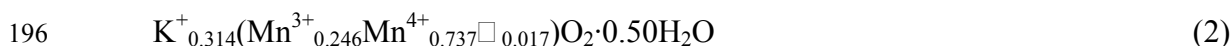
179

180 **Chemical Analyses and Structural Formulae.**

181 *Amount of Interlayer Water.* The DTA curve of KBi₁₀ contains two endotherms at 178°C
182 and 926°C, respectively (Fig. 1). The low-temperature endotherm (178°C) corresponds to the
183 loss of weight due to interlayer water, whose amount equals 7.5 wt% (between 120-210°C)
184 while the high-temperature endotherm (926°C) is likely related to KBi melting. The
185 additional loss of weight within the 60-120°C range is most likely related to water adsorbed
186 on grain surfaces. In contrast to what was observed for sample KBi₈ and hydrothermal
187 birnessite [67,77], no DT peak or change of slope in TG curve were observed over the 250-
188 400°C interval.

189 *Structural Formula.* The K/Mn atomic ratio [$y = 0.320(5)$] was calculated from K and Mn
190 ICP concentrations values measured from the same solution whereas the H₂O/Mn mole ratio
191 (0.50) was deduced from the weight loss measured between 120°C and 210°C and
192 corresponding to the loss of interlayer water. Chemical analyses have shown that the mean
193 oxidation degree was equal to 3.75(2). Using these values and eq 1 the following structural

194 formula, in which □ correspond to vacant layer sites, can be deduced for KBi₁₀ crystals at
195 room temperature and pressure:



197 **Indexing of the experimental XRD patterns.**

198 *Sample KBi₁₀*. The powder XRD pattern (Fig. 2A) contains a rational series of basal
199 reflections with $d(00l)$ values corresponding to a minimum periodicity along the \mathbf{c}^* axis equal
200 to 7.044 Å. The non-basal reflections are intense and sharp. The positions of hkl reflections
201 are compatible with an orthorhombic two-layer ($2O$) C -centered cell with $a = 5.1554(3)$ Å,
202 $b = 2.8460(1)$ Å, $c = 14.088(1)$ Å, $\alpha = \beta = \gamma = 90^\circ$, $a/b = \sqrt{3.281}$ (Table 1). With such an
203 indexing, XRD patterns of birnessites contain $20l/11l$ reflections over the $34\text{-}64^\circ$ 2θ $\text{CuK}\alpha$
204 angular range, $31l/02l$ maxima being visible over the $64\text{-}74^\circ$ 2θ $\text{CuK}\alpha$ range and $40l/22l$ over
205 the $74\text{-}90^\circ$ 2θ range. Along with the described hkl reflections, the XRD pattern contains
206 additional weaker reflections, mainly over the $5\text{-}34^\circ$ 2θ region (inset on Fig. 2A), which can
207 be indexed using a C -centered supercell with $A = 3a$, $B = b$, $C = c$, $\alpha = \beta = \gamma = 90^\circ$. This
208 super-structure will be described and its origin discussed in the final part of this four paper
209 series [66].

210 *Sample 100-KBi₁₀*. The XRD pattern of 100-KBi₁₀ (Fig. 2B) is very similar to that of
211 KBi₁₀ and can be indexed with a $2O$ unit cell (Table 1). Previously described super-reflections
212 are still visible.

213 *Sample 150-KBi₁₀*. Although TD-TG curves indicate that KBi₁₀ dehydrates essentially at
214 $\sim 180^\circ\text{C}$, the XRD pattern of 150-KBi₁₀ (Fig. 2C) shows a significant decrease of the $d(002)$
215 value at ~ 6.44 Å, and related shifts of hkl reflections. The higher temperature deduced from
216 TD-TG curves for the departure of interlayer H₂O molecules likely results from the high
217 heating rate used for the thermal analysis, whereas the 2-hour plateau at 150°C likely allowed
218 reaching complete dehydration before XRD data collection. Apart from the reduction of the
219 unit-cell dimension along the \mathbf{c}^* axis, the birnessite layer structure remains essentially stable,

220 the main reflections being indexed with a $2O$ unit cell (Table 1). A close look at the
221 experimental XRD pattern reveals however that the profile of intense non-basal reflections is
222 altered with shoulders visible on their low-angle sides (shown for the 114 reflection on the
223 inset – Fig. 2C). These additional maxima can be indexed using a two-layer hexagonal ($2H$)
224 unit cell with $a = 5.010(3) \text{ \AA}$, $b = 2.891(1) \text{ \AA}$, $c = 12.871(4) \text{ \AA}$, $\alpha = \beta = \gamma = 90^\circ$, $a/b = \sqrt{3.00}$
225 (Table 1). Additional low-intensity peaks visible over the $5\text{-}30^\circ 2\theta$ range can be indexed
226 using a C -centered supercell with $A = 3a$, $B = 3b$, $C = c$, $\alpha = \beta = \gamma = 90^\circ$.

227 *Samples 250-KBi₁₀ and 350-KBi₁₀.* At 250°C dehydration is complete and heating of
228 KBi_{10} at this temperature dramatically modifies the experimental XRD pattern as the result of
229 important structural changes that persist at least up to 350°C , XRD patterns of both 350-KBi_{10}
230 and 250-KBi_{10} being similar (Figs 2D-E). The two patterns contain two basal reflections
231 characteristic of birnessite together with a set of intense and sharp non-basal reflections
232 showing that the structural perfection is preserved. However, the orthogonal symmetry of the
233 low-temperature KBi_{10} layers is transformed into a hexagonal one for samples 250-KBi_{10} and
234 350-KBi_{10} , hkl reflections being then indexed using a two-layer hexagonal unit cell ($2H$ –
235 Table 1). XRD patterns of samples 250-KBi_{10} and 350-KBi_{10} also contain weak super-
236 reflections in the $5\text{-}35^\circ 2\theta$ range that are similar to those observed at 150°C and indexed using
237 a C -centered $A = 3a$, $B = 3b$, $C = c$, $\alpha = \beta = \gamma = 90^\circ$ supercell.

238 *Sample AfterT-KBi₁₀.* Reflections present in the experimental XRD patterns of KBi_{10}
239 specimens recorded at room temperature before and after heating at 350°C (Figs. 2A and 2F,
240 respectively) have similar positions and intensities. This means that the structural
241 modification undergone during the heating at 350°C is essentially reversible. The increase of
242 the minimum periodicity along the \mathbf{c}^* axis from 6.42 \AA back to 7.02 \AA after cooling of the
243 sample shows that birnessite layers re-hydrate. The orthogonal layer symmetry is also
244 recovered, reflections of sample AfterT- KBi_{10} being indexed with a two-layer orthorhombic
245 unit cell ($2O$ – Table 1). Super-reflections corresponding to the initial $A = 3a$, $B = b$, $C = c$,

246 $\alpha = \beta = \gamma = 90^\circ$ *C*-centered supercell are also recovered. However, differences are visible
 247 between KBi_{10} and AfterT- KBi_{10} patterns. In particular, in the latter pattern $20l$ reflections are
 248 broader and their intensity relative to the $11l$ reflections (with the same l index) significantly
 249 dropped as compared to sample KBi_{10} (Figs. 2A, 2F and 3). This effect was described in
 250 details by Gaillot et al. for the heterogeneous $\text{KBi}_{10\text{h}}$ variety obtained at 1000°C [68]. It was
 251 shown that $20l$ reflection broadening and weakening are linked to the coexistence of several
 252 populations of KBi particles. All populations are $2O$ modifications with slightly different a
 253 and b parameters that are related by the equation:

$$254 \quad \frac{1}{d(110)^2} = \frac{1}{a_i^2} + \frac{1}{b_i^2} \quad (3)$$

255 As a consequence, positions of $11l$ reflections are insensitive to the variation of unit-cell
 256 parameters, whereas $20l$ reflections of individual $2O$ modifications are slightly shifted. The
 257 resulting overlap of $20l$ reflections from different $2O$ modifications broadens the resulting
 258 diffraction maxima, peak broadening decreasing with increasing l values (solid circles, Fig.
 259 3).

260 *Sample Vacuum-KBi₁₀*. The XRD pattern of Vacuum- KBi_{10} is very similar to that of 150-
 261 KBi_{10} and presents a shift of basal reflections from 7.044 \AA down to 6.397 \AA , suggesting the
 262 departure of $\text{H}_2\text{O}_{\text{interlayer}}$ (Fig. 2G). As for 150- KBi_{10} , hkl reflections are similar to those of
 263 KBi_{10} but shifted towards higher angles. In contrast to sample 150- KBi_{10} , no reflections
 264 corresponding to a $2H$ modification are visible, all reflections being indexed with a unique $2O$
 265 unit cell (Table 1). Additional weak reflections correspond to a *C*-centered supercell with $A =$
 266 $3a$, $B = 3b$, $C = c$, $\alpha = \beta = \gamma = 90^\circ$. Finally, two additional very weak maxima at 6.964 \AA and
 267 3.486 \AA likely correspond to basal reflections corresponding to a few partially hydrated
 268 crystals.

269 *AfterVac-KBi₁₀*. The XRD pattern is very similar to that of KBi_{10} with the 002 basal
 270 reflection shifted back from 6.397 \AA to 7.038 \AA indicating the reversibility of the dehydration
 271 process. Reflections are indexed using a $2O$ unit cell with parameters very similar to those

272 obtained before dehydration (Table 1). Visible super-reflections correspond to the initial C-
273 centered supercell with $A = 3a$, $B = b$, $C = c$, $\alpha = \beta = \gamma = 90^\circ$.

274 Unit-cell parameters for all KBi_{10} samples can be found in Table 1, indexation of
275 experimental diffraction lines being provided as supplementary material.

276 **Structure Refinement of KBi_{10} Subcells.**

277 *Rietveld Refinement of KBi_{10} Subcell.* On KBi_{10} XRD pattern all hkl reflections
278 consistently have low full width at half maximum intensity (fwhm). In particular, after
279 correction for crystal-size broadening by a $\cos\theta$ factor [78], fwhm of $11l$ reflections only
280 slightly increases with increasing l values (from 0.125° to 0.165° 2θ – open triangles, Fig. 3)
281 whereas that of $20l$ reflections is independent of l (0.165° 2θ – open circles, Fig. 3). This data
282 indicates the high structural perfection of KBi_{10} . Small angular regions containing weak
283 super-reflections (at $\sim 37.5^\circ$, $\sim 39.5^\circ$ and $\sim 51.0^\circ$ 2θ) were excluded from the Rietveld
284 refinement. Atomic positions of KBi_{10} subcell were refined using space group $Ccmm$. Initial
285 occupancies of structural sites correspond to the structural formula of KBi_{10} (eq 2). In the
286 initial model schematized on Fig. 4A Mn_{layer} are located at the subcell origin, and O_{layer} have
287 coordinates (0.333, 0, 0.071) to match the ~ 2.00 Å layer thickness previously refined for
288 several synthetic birnessite structures [5,8,58,67,77,79]. K^+ are located in the interlayer mid-
289 plane, above and below the layer empty tridentate cavities, sharing three edges with octahedra
290 of adjacent layers (TE sites – Fig. 4A), whereas $\text{H}_2\text{O}_{\text{interlayer}}$ are located in-between the nearest
291 O_{layer} from adjacent layers. At this stage $R_{\text{wp}} = 22.65\%$ and $R_{\text{B}} = 23.45\%$. All structural
292 parameters were then successively refined, starting from unit-cell parameters, PSFs (the width
293 of basal reflections $00l$ and non-basal hkl reflections being described by two sets of
294 parameters) and preferential orientation. Atomic positions and occupancies were then refined.
295 As compared to the initial structure model O_{layer} and $\text{H}_2\text{O}_{\text{interlayer}}$ were shifted along the **a** axis
296 from the initial positions. In addition, the K site was split between three positions located
297 within the interlayer prismatic cavity ($R_{\text{wp}} = 12.52\%$, $R_{\text{B}} = 9.57\%$). At this stage, calculated

298 20l and 11l reflections are slightly more and less intense, respectively, than corresponding
299 experimental reflections. As 20l fwhm values are slightly higher than those of 11l ones (solid
300 circles and solid triangles, respectively – Fig. 3A) some KBi₁₀ particles likely have unit-cell
301 parameters differing from those of the major part of the sample, unit-cell parameters from the
302 different populations following eq 3.

303 To better fit the broader 20l reflections, two PSFs were thus considered for 20l/31l/40l
304 and 11l/02l/22l diffraction lines, respectively, and structural parameters were refined again.
305 The use of two PSFs allowed fitting better the width of all *hkl* reflections, but did not affect
306 significantly the details of the optimum structure model, whose main parameters are listed in
307 Table 2. The refined site atomic coordinates and occupancies given in Table 3 led to the
308 optimum fit shown in Fig. 5A ($R_{wp} = 11.21\%$, $R_B = 5.50\%$ – Table 2). Selected interatomic
309 distances are listed in Table 4. Consistently with the calculated structural formula (eq 1),
310 KBi₁₀ consists of vacancy-free layers, the refined Mn_{layer} occupancy being very close to 1.0
311 (0.985). Deviation of layer symmetry from the hexagonal one induces a significant shift of
312 O_{layer} from the ideal anion close-packing sites [(0.342, 0, 0.070) – Table 3]. This position is
313 similar to that of O_{layer} in Mn³⁺-bearing birnessite varieties exhibiting an orthogonal layer
314 symmetry [5,8,70]. The refined K⁺ site is split into three ones each being shifted in the **ab**
315 plane from the center of the interlayer prism towards its faces [(-0.253, 0, 0.25) and (-0.134,
316 ±0.375, 0.25) – Fig. 4C, Table 3]. Similar positions were obtained if K⁺ was initially located
317 at the center of prism faces. Similar K⁺ positions were found for KBi₈ and hydrothermal KBi
318 [67,77]. H₂O_{interlayer} are also slightly shifted in the **ab** plane from their initial positions to form
319 a 132.9(3)° angle with the two nearest O_{layer} from adjacent layers [(0.127, 0, 0.25) – Figs 4C-
320 D]. All attempts to split the H₂O_{interlayer} site from the edge of the prismatic cavity along [100],
321 [110] and [1 $\bar{1}$ 0] failed, the site along the **a** direction being systematically the sole with a final
322 significant occupancy.

323 *Rietveld Refinement of 350-KBi₁₀ Subcell.* The initial model was deduced from the
324 refined KBi₁₀ model, but 350-KBi₁₀ layers were considered to have a hexagonal symmetry,
325 the structure being described in the *P6₃/mmc* space group. O_{layer} were first assumed to be
326 located in (1/3, 0, 0.078), K⁺ positions and occupancies were kept as in KBi₁₀, and no
327 H₂O_{interlayer} was introduced according to TD-TG results. Structural parameters leading to the
328 best fit between experimental and calculated XRD patterns (Fig. 5B – $R_{wp} = 16.80\%$, $R_B =$
329 13.22%) are given in Table 3 whereas selected interatomic distances are listed in Table 4. As
330 for KBi₁₀, 350-KBi₁₀ layers are essentially devoid of vacancies as the occupancy refined for
331 Mn_{layer} is close to 1.0 (0.983), in agreement with the structural formula proposed for KBi₁₀ (eq
332 2). Due to the hexagonal layer symmetry O_{layer} are no longer shifted from the ideal anion
333 close-packing sites [(0.333, 0, 0.079) – Table 3]. Note however that this position was highly
334 unstable when refined. As discussed below this instability may arise from the presence in the
335 layers of Mn³⁺-octahedra with their long Mn³⁺-O bonds randomly oriented with respect to the
336 **a** axis. As for KBi₁₀ at room temperature, the refined K⁺ site is split into three positions,
337 equivalent to (-0.300, 0, 0.25), shifted in the **ab** plane from the prism's center toward one of
338 its faces. Compared to KBi₁₀ structure this position is closer to the prism's center likely to
339 provide reasonable K-O_{layer} distances (2.73 Å *vs* 2.97 Å, for 350-KBi₁₀ and KBi₁₀,
340 respectively) despite the interlayer collapse [77].

341 *Structure of Heated KBi₁₀ Samples.* Between 100°C and 150°C a 2*O*-to-2*H* structural
342 transformation occurs as described in the indexation section. The structure of 100-KBi₁₀ is
343 assumed to be identical to the 2*O* modification of KBi₁₀ whereas 150-KBi₁₀ can be considered
344 as a physical mixture of hydrated 2*O* and dehydrated 2*H* structures (similar to samples KBi₁₀
345 and 350-KBi₁₀, respectively). At 250°C, dehydration and 2*O*-to-2*H* structural changes are
346 complete, and the structure of sample 250-KBi₁₀ was assumed to be identical to that of 350-
347 KBi₁₀. No structural refinement was performed on these three samples.

348 *Rietveld Refinement of Vacuum-KBi₁₀ Subcell.* As for KBi₁₀, small angular regions
349 containing super-reflections (at ~43.5° and ~52.0° 2θ) were excluded from the refinement.
350 The initial structure model was identical to that of KBi₁₀ without H₂O_{interlayer} in agreement
351 with the dehydration under deep vacuum conditions. As for KBi₁₀, two PSFs were used to
352 account for the increased width of 20l/31l/40l diffraction lines compared to 11l/02l/22l ones.
353 The best fit is shown on Fig. 5C ($R_{wp} = 10.91\%$, $R_B = 6.85\%$). Refined O_{layer} positions (0.341,
354 0, 0.076) are similar to those in the original model, while refined K⁺ positions are moved
355 toward the prism's center [(-0.300, 0, 0.25) and (0.153, ±0.459, 0.25)], as found for sample
356 350-KBi₁₀. Refined structural parameters and selected inter-atomic distances are listed in
357 Tables 2 and 3, respectively.

358 **Qualitative and Quantitative Analysis of the EXAFS Spectra of KBi₁₀ and Related**
359 **Synthetic Birnessites.** The short range order of Mn in KBi₁₀ was determined by using
360 synthetic Na- and H-birnessite (hereafter referred to as NaBi and HBi, respectively) as
361 references. The crystal structures of NaBi and HBi were determined by X-ray and electron
362 diffraction and EXAFS spectroscopy [8,46,47,80]. Triclinic NaBi consists of vacancy-free
363 Mn layers and its structural formula is Na⁺_{0.31}(Mn⁴⁺_{0.69}Mn³⁺_{0.31})O₂·0.40H₂O. Mn³⁺ octahedra,
364 which are elongated by the Jahn-Teller effect, are ordered in rows along [010] that are
365 separated by two Mn⁴⁺ rows along [100]. Due to this cation ordering and the distortion of the
366 Mn³⁺ octahedra, the layer symmetry departs from hexagonal to orthogonal [8,46]. The
367 structural formula of HBi at pH4 is
368 H⁺_{0.33}Mn²⁺_{0.043}Mn³⁺_{0.123}(Mn⁴⁺_{0.722}Mn³⁺_{0.111}□_{0.167})O₂(OH)_{0.013}, where □ represents vacancies
369 [80]. Its layer contains much less Mn³⁺ than NaBi (13% Vs. 31%) and, as a consequence, it
370 has a hexagonal symmetry. HBi structure also differs from that of NaBi by the presence of
371 cationic layer vacancies, which are capped by interlayer Mn³⁺ and Mn²⁺ cations. As a result,
372 NaBi has only edge-sharing Mn_{layer} octahedra whereas HBi contains in addition corner-
373 sharing Mn_{interlayer}-Mn_{layer} pairs with a distance separation of about 3.52 Å. Another important

374 distinction between these two references is that the $\text{Mn}_{\text{layer}}\text{-Mn}_{\text{layer}}$ EXAFS distances are equal
375 in HBi (2.89 Å) and unequal in NaBi (2.89 and 3.01 Å) [67], owing to the hexagonal V_s
376 orthogonal layer symmetry.

377 Figs. 6A-B show that the resonance at $k = 8.05 \text{ \AA}^{-1}$ in HBi is split in two maxima at 7.8
378 and 8.1-8.2 Å^{-1} in NaBi and KBi_{10} . Previous studies have shown that this indicator region is
379 sensitive to the amount and ordering of $\text{Mn}^{3+}_{\text{layer}}$ [67,81-83]. When the layer has no Mn^{3+} , the
380 resonance peaks at 8.05 Å^{-1} . When it contains 1/3 Mn^{3+} and 2/3 Mn^{4+} , and the Mn^{3+} cations
381 are not orderly distributed in rows, as in lithiophorite, then the hexagonal symmetry of the
382 layer is preserved and the resonance is shifted to lower k values (higher interatomic
383 distances), peaking at 7.9 Å^{-1} [83]. In contrast, the resonance is split when the Mn-Mn
384 distances have essentially a bimodal distribution, that is when $\text{Mn}^{3+}_{\text{layer}}$ are segregated in
385 rows. Using that spectroscopic feature as a structural fingerprint for Mn ordering in
386 phyllomanganates, KBi_{10} and NaBi have the same $\text{Mn}^{3+}\text{-Mn}^{4+}$ distribution patterns. The
387 absence of interlayer Mn atoms follows also from the comparison of the RSFs for KBi_{10} ,
388 NaBi and HBi (Figs. 6C-D). The corner-sharing $\text{Mn}_{\text{interlayer}}\text{-Mn}_{\text{layer}}$ correlation gives a peak at
389 $R + \Delta = 3.1 \text{ \AA}$ [47,84], observed in HBi but neither in NaBi nor in KBi_{10} . Although Mn
390 clearly has a similar environment in KBi_{10} and NaBi, the average bond lengths at the Mn site
391 are not strictly identical. The EXAFS spectrum of KBi_{10} is shifted towards the high k values
392 relative to NaBi (Fig. 6A), and this frequency modification induces a left-shift of the
393 imaginary part of the Mn shells in the real space (Fig. 6E). Comparing the imaginary parts for
394 the three phyllomanganates, we find that the average Mn-Mn distances decreases from NaBi,
395 to KBi_{10} , to HBi (Figs. 6E-F). This trend is consistent with the evolution of the fractional
396 amounts of $\text{Mn}^{3+}_{\text{layer}}$ in the three compounds: 0.31 in NaBi, 0.25 in KBi_{10} , and 0.13 in HBi.
397 The O shell has lesser sensitivity than the Mn shell to the amount of $\text{Mn}^{3+}_{\text{layer}}$ because the four
398 equatorial $\text{Mn}^{3+}\text{-O}$ distances ($\sim 1.93 \text{ \AA}$) [85], are similar to the $\text{Mn}^{4+}\text{-O}$ distances ($\sim 1.91\text{-}$
399 1.92 \AA) [47,76,86], and because the two distant $\text{Mn}^{3+}\text{-O}$ pairs at 2.2-2.3 Å make a low

400 contribution to the total EXAFS signal (33% of the Mn-O pairs for 25% of the Mn cations,
401 that is 8% of the total Mn-O pairs) [47]. Still, close examination of Figs. 6E-F shows that the
402 imaginary part of the O shell for KBi₁₀ is superimposed to that for HBi, but slightly left-
403 shifted relative to that for NaBi. Consistently, the best-fit Mn-O EXAFS distance for KBi₁₀
404 was equal to 1.91 Å as in HBi, 0.01 Å shorter than in NaBi (Table 5). The similarity of the O
405 shell parameters for KBi₁₀ and HBi is explained with reference to the fact that the first RSF
406 peaks are the weighted sum from all the Mn atoms present in the structure. When Mn_{layer} and
407 Mn_{interlayer} atoms in HBi are added, then HBi and KBi₁₀ have almost the same Mn³⁺/Mn_{total}
408 ratio (0.24 Vs. 0.25).

409 Similarly to NaBi, a two-shell fit to the Mn-Mn contribution provided an optimal
410 simulation to the data (Table 5). The short-distance Mn-Mn correlation at 2.89 Å is attributed
411 to the Mn⁴⁺-Mn⁴⁺ and Mn³⁺-Mn³⁺ pairs, and the long-distance Mn-Mn correlation at ~3.01-
412 3.02 Å to the Mn⁴⁺-Mn³⁺ pairs [47]. In NaBi, the first subshell contains about 3.6 atoms and
413 the second about 2.4, while they contain about 3.5 and 1.6 atoms in KBi₁₀, respectively.
414 Although the differences in coordination numbers between the two samples are within
415 accuracy, the apparent decrease of the number of the long-distance pairs in KBi₁₀ is consistent
416 with the decrease of its Mn³⁺ content. The fact that the double antinode at ~8 Å⁻¹ is less
417 pronounced in KBi₁₀ than in NaBi (Fig. 6A) is definite evidence of the attenuation of the Mn
418 shell splitting caused by lower amounts of Mn³⁺.

419 Overall, the structure models proposed here for KBi₁₀, and previously for HBi and NaBi
420 [47], are consistent with XRD and EXAFS data. Upon closer examination, however, it
421 appears that EXAFS gives shorter Mn-O and longer Mn-Mn distances than XRD, and that the
422 number of oxygens in the first shell often is lower than six (Tables 3, 4 and 5). The
423 discrepancy between the first shell structural parameters derived by the two techniques has a
424 simple explanation. In Mn³⁺-containing phyllosulfates, the distribution of Mn-O distances
425 is broad (from ~1.91 Å to 2.2-2.3 Å) and highly asymmetrical due to the elongation of the

426 Mn^{3+} octahedra. When the interlayer contains Mn atoms, as in HBi, the interlayer Mn-O and
427 Mn-H₂O distances are longer than the average Mn-O distance in the layer (Table 6). In these
428 mixed-valency and multi Mn sites compounds, the EXAFS analysis of the O shell with a
429 standard Gaussian-shell model excludes the full distribution of interatomic distances [87].
430 Since the tail of the distance separation is stretched towards higher R values (e.g., 2.2-2.3 Å
431 for Mn^{3+} and 1.98-2.08 Å for interlayer Mn), analysis of the data using symmetrical
432 distributions leads to lower numbers of O atoms around each Mn atom, and the EXAFS-
433 derived $\langle \text{Mn-O} \rangle$ distance is thus shorter than the weighted average crystallographic value.
434 Cumulant analysis was tested in the present study but proved unsuccessful to detect the “lost”
435 atoms, because the tail apparently does not die off fast enough for cumulants of high orders to
436 be neglected (i.e., the asymmetry is too high).

437 This complication is circumvented sometimes in the literature by fixing the total number
438 of oxygens (CN) to six in the spectral fits [88,89]. This modelling strategy is inappropriate
439 when the structural disorder is high because the effective number of oxygen atoms detected
440 by EXAFS in the harmonic approximation is lower than six. In a recent study, the O shell of a
441 series of phyllophanates was fitted with two Gaussian functions centred at 1.85-1.89 Å and
442 1.90-1.94 Å, and by constraining $CN = 6$ (Table 6) [90]. However, the distance separation
443 between the two functions is not high enough to include the longer bond lengths and the total
444 number of oxygens which can be recovered by this alternative model is thus lower than six.
445 For example, in NaBi, the number of oxygens at short distance is $0.69 \times 6 + 0.31 \times 4 = 5.4$. In
446 this recent study, the analysis of the Mn shell is also problematic for three reasons (Table 6).
447 First, NaBi does not have corner-sharing Mn octahedra. Second, if 0.8 Mn-Mn_{corner} pairs were
448 present in this compound, as assumed from EXAFS, then the number of Mn-Mn_{edge} pairs
449 should be lower than six, since interlayer Mn octahedra do not share edges with other Mn
450 octahedra. The same reasoning applies to HBi. Although this compound actually contains
451 interlayer Mn, the number of Mn-Mn_{edge} pairs was arbitrarily fixed to six by the authors. The

452 average number of Mn-Mn_{edge} pairs in HBi can be calculated from its structure as the
453 weighted sum of the different environments:

$$454 \quad CN_{\text{edge}} = \sum_i W_i CN_i \quad (4)$$

455 where i refers to Mn site, W_i to Mn site occupancy, and CN_i to the number of Mn neighbors
456 for site i . For HBi, $CN_{\text{edge}} = 0.666 \times 4 + 0.166 \times 5 = 3.5$, as there are 50% vacancies in the
457 Mn³⁺-rich rows, and each Mn in these rows is surrounded by five Mn [47]. Our EXAFS CN
458 value for KBi₁₀ (4.8) agrees with theory (3.5) within accuracy, but not the prescribed value of
459 six in the alternative model. Third, the Mn-Mn edge-sharing distances are split in NaBi, due
460 to the orthogonal symmetry of the layer, but not in HBi, whose layer symmetry is hexagonal.
461 From XRD data, the distance separation in NaBi is $2.95 - 2.85 = 0.10 \text{ \AA}$ (Table 6). In the
462 alternative EXAFS model, the distance separation in NaBi is as small as $2.90 - 2.88 = 0.02 \text{ \AA}$
463 and, thus, incompatible with the orthogonal layer symmetry. The results reported for HBi are
464 even more questionable: not only the Mn-Mn distances were assumed to be split but, in
465 addition, in an amount ($2.89 - 2.84 = 0.05 \text{ \AA}$) higher than in NaBi.

466 The Mn-Mn edge-sharing distances obtained here by EXAFS for HBi (2.89 \AA) and NaBi
467 ($2.89 + 3.01 \text{ \AA}$) are $\sim 0.04 \text{ \AA}$ longer than those obtained by XRD (2.85 \AA and $2.85 + 2.95 \text{ \AA}$,
468 respectively – Tables 4 and 5). This difference is regarded as significant as EXAFS and XRD
469 give the same Mn-Mn distance in λ -MnO₂. The discrepancy between the lattice parameter
470 values (XRD) and the cation-cation distances (EXAFS) can be reconciled by considering that
471 the octahedral layer is corrugated. In increasing the Mn-Mn distance, the buckling of the
472 octahedral layer minimizes the cationic repulsion and contributes to increase the layer
473 stability. This effect has been described first in hydrotalcite by combining XRD, anomalous
474 scattering and EXAFS spectroscopy [91], and was subsequently inferred to occur also in
475 birnessite from the quantitative analysis of the long distance Mn-Mn-Mn multiple scattering
476 paths in EXAFS [90,92], The angular deviation from the layer planarity, as estimated from

477 the difference of the EXAFS and XRD distances, is $\alpha = \cos^{-1}(2.85/2.89) \sim \cos^{-1}(2.95/3.01) \sim$
478 $10.5(10)^\circ$ in HBi and NaBi.

479

480

Discussion

481

482 The structure of high-temperature KBi synthesized at 1000°C (KBi₁₀ – this study) differs
483 substantially from that of KBi obtained at 800°C (KBi₈), whose structure was described in the
484 first of this four paper series [67]. Differences in chemical composition, layer symmetry and
485 origin of the layer charge between KBi₈ and KBi₁₀ are discussed first. Then, the nature of
486 structural modifications induced by thermal treatment at 350°C of KBi₁₀ is examined. From
487 these considerations and the comparison with structural features of other birnessites and layer
488 Mn oxyhydroxides, a generalized relationship between the layer symmetry and the origin of
489 the layer charge is proposed. Finally, the possible modification of the layer and interlayer
490 structure of KBi₁₀ in vacuum is discussed, and supporting arguments for the relevance of
491 SAED to study KBi₁₀ structure are presented.

492

Structure Model for KBi₁₀ Sample.

493 *Chemical Composition of KBi₁₀ Layers and Layer Symmetry.* One of the major differences
494 between KBi₈ and KBi₁₀ is their layer symmetry, as reflected by their *a/b* ratios ($1.732 = \sqrt{3}$
495 and $1.811 = \sqrt{3.28}$, respectively) [67]. Drits et al. showed that the symmetry of the
496 phyllomanganate layers departs from being hexagonal when Mn³⁺ and Mn⁴⁺ cations are
497 orderly distributed in rows parallel to the **b** axis, Jahn-Teller distorted Mn³⁺ octahedra being
498 systematically elongated along the **a** axis (cooperative Jahn-Teller effect) [46]. The ordering
499 of heterovalent Mn cations in birnessite layers is energetically favorable as it minimizes the
500 steric strain induced by the presence of high amounts of distorted Mn³⁺ octahedra. In this
501 case, the unit-cell *b* dimension (2.84-2.86 Å) is not significantly modified because the **b**
502 direction is perpendicular to the direction of elongation of the Mn³⁺ octahedra and the Mn⁴⁺-O

503 and the four equatorial Mn³⁺-O distances are equivalent. In contrast, the unit-cell *a* dimension
504 is increased and, consequently, the *a/b* ratio varies as a function of the Mn³⁺/Mn⁴⁺ ratio in the
505 octahedral layer. For example, in crednerite (CuMnO₂) *a/b* = 1.936 (Mn³⁺ = 100 %) [85], in
506 Na-rich busserite *a/b* = 1.835 (Mn³⁺ = 33 %) [70], in Na-rich birnessite *a/b* = 1.817 (Mn³⁺ =
507 31 %) [5,8,46], and in Ca-rich birnessite *a/b* = 1.808 (Mn³⁺ = 22%) [70]. Thus, the *a/b* ratio is
508 an indicator of the unique orientation of the elongated Mn³⁺ octahedra (cooperative Jahn-
509 Teller effect) sensitive to the Mn³⁺/Mn_{total} ratio in the layer when Mn³⁺ cations are ordered in
510 rows. Note that in lithiophorite [(Al³⁺_{0.67}Li⁺_{0.32})(Mn⁴⁺_{0.68}Mn³⁺_{0.32})O₂(OH)₂], which contains
511 32% of layer Mn³⁺, the hexagonal symmetry of the layer is preserved (*a/b* = √3) because the
512 Mn³⁺ octahedra are elongated along three directions in the **ab** plane [83]. Thus, both the *a* and
513 *b* dimensions are enlarged relative to Mn³⁺-free layers (*b* = 2.925 Å Vs. 2.842-2.850 Å) [93].

514 KBi₁₀ provides new evidence for the relationship between the *a/b* and the Mn³⁺/Mn_{total}
515 ratios when the layer symmetry is orthogonal, as both its *a/b* ratio (1.811) and chemical
516 analysis indicate that it contains less Mn³⁺ than NaBi (0.25 Vs. 0.31) and that they are ordered
517 and systematically elongated along one direction. This finding is supported also by the
518 shallowness of the “dunce's cap” feature at ~8 Å⁻¹ and the lower frequency of the EXAFS
519 spectrum for KBi₁₀ compared to NaBi (Fig. 6A). Lanson et al. showed that the amount of
520 layer Mn³⁺ could be estimated from the <Mn-O> distance, taking as end-members <d(Mn³⁺-
521 O)> = 2.04 Å, as calculated from crednerite and Mn oxyhydroxides, and <d(Mn⁴⁺-O)> =
522 1.912 Å, as calculated for λ-MnO₂ and hydrothermal birnessite (KBi_{hydr}) [8,76,77,85,94]. The
523 <Mn-O> distance calculated for the (Mn⁴⁺_{0.75}Mn³⁺_{0.25}) layer cation composition of KBi₁₀
524 (1.950 Å) is close to the experimental value (1.949 Å – Table 4). Similarly, the long Mn-O
525 distance calculated as the weighted sum of the Mn⁴⁺-O distance (1.912 Å in λ-MnO₂) and of
526 the long Mn³⁺-O distance (2.26 Å in crednerite) is 1.999 Å, and agrees with the XRD value
527 (2.021 Å – Table 4).

528 *Chemical Composition of KBi₁₀ Layers and Origin of the Layer Charge.* Another
529 important difference between KBi₈ and KBi₁₀ is the origin of their layer charge. KBi₈ has a
530 layer charge, which arises uniquely from cationic vacancies since the layer has no Mn³⁺
531 cations. This charge is compensated for by the binding of Mn³⁺_{interlayer} at vacancy sites and the
532 sorption of K⁺ [67]. In contrast, the layer charge deficit in KBi₁₀ arises mostly from the
533 substitution of 0.25 Mn⁴⁺_{layer} by the same mole fraction of Mn³⁺_{layer} and is compensated by
534 0.31 K⁺ in the interlayer. According to XRD, layers are almost vacancy free. Additional
535 support for the absence of layer vacancies in KBi₁₀ follows from EXAFS results. Quantitative
536 analysis of the double antinode at ~8 Å⁻¹ has shown that its unique “dunce's cap” shape
537 resulted from multiple scattering paths of the photoelectron between four aligned Mn shells in
538 the layer plane [83]. This high-order pair correlation, up to an effective radial distance of
539 ~2.90 × 3 = 8.7 Å, can only be observed if the three successive Mn positions around a central
540 Mn site are filled.

541 **Layer Symmetry and Orientation of Mn³⁺ Octahedra in Sample 350-KBi₁₀.** Structure
542 models of KBi₁₀ at room temperature and at 350°C differ by their layer symmetries and,
543 consequently, by their unit-cell parameters and interatomic distances. The in-plane layer cell
544 parameters for hexagonal 350-KBi₁₀ ($b = 2.894$ Å – Table 1) are significantly higher than
545 those for hexagonal (1*H* and 2*H*) birnessites (2.844-2.848 Å at room temperature)
546 [58,67,80,95]. As a result, 350-KBi₁₀ has a longer <d(Mn-O)> (1.956 Å – Table 4) than 1*H*
547 and 2*H* birnessites at room temperature (~1.91 Å) but, for steric reasons, it still coincides with
548 the average distance in KBi₁₀ (1.949 Å – Table 4), since the two samples likely have the same
549 Mn³⁺/Mn_{total} ratio. The slight increase of the <Mn-O> distance (from 1.949 to 1.956 Å, for
550 KBi₁₀ and 350-KBi₁₀, respectively) likely is likely related to thermal expansion.

551 One likely explanation for the layer symmetry modification with thermal treatment is a
552 change of the azimuthal orientation of the elongation axes of the Mn³⁺ octahedra. If these axes
553 are oriented with equal probability at ± $n120^\circ$ (n integer) directions, the resulting layer

554 symmetry is hexagonal. This configuration likely distorts locally the O_{layer} lattice, and may
555 explain the instability of the O_{layer} position during the structure refinement of 350-KBi₁₀.
556 Random orientation of Mn^{3+} octahedra induces unfavorable lattice strains that are likely
557 compensated for by the thermal energy available at 350°C. Such random distribution of Mn^{3+}
558 octahedra azimuthal orientation induces a significant increase of the unit-cell b parameter as
559 compared to that measured for vacancy-free layers or for layers with a unique orientation of
560 the long Mn^{3+} -O bonds in the **ac** plane. As mentioned above, such large b unit-cell dimension
561 was reported for lithiophorite ($b = 2.912 \text{ \AA}$) [93] whose layers have a preserved hexagonal
562 symmetry due to the random orientation of the Mn^{3+} octahedra in the **ab** plane [83].
563 Consistently, the b parameter determined for 350-KBi₁₀ is increased compared to KBi₁₀
564 (2.895 and 2.846 \AA , respectively). As described by Gaillot et al. for hydrothermal KBi
565 samples [77], this abrupt increase with increasing temperature (Table 1) cannot result solely
566 from thermal motion as the unit-cell dilatation usually depends linearly on the temperature if
567 the structure is not modified. The $2O$ -to- $2H$ transition with an increase of the b parameter
568 (from 2.846 to 2.895 \AA) observed above 150°C can thus be considered as a direct evidence for
569 the presence of a significant amount of Mn^{3+} octahedra in KBi₁₀ layers and for their
570 systematic elongation along the **a** axis at room temperature.

571 **General Relationship Between Layer Symmetry and Origin of the Layer Charge in**
572 **Birnessites.** The comparison between structural features of KBi₈, KBi₁₀ and 350-KBi₁₀ can be
573 extended to all birnessite varieties, allowing general relationships between layer symmetry,
574 layer cation composition, $\langle Mn-O \rangle$ distance and the origin of the layer charge to be drawn.
575 HBi, KBi₈, KBi_{hydr} are characterized by low amounts of Mn^{3+}_{layer} , high layer vacancy contents
576 being responsible for the layer charge deficit. As a result, these species exhibit short $\langle Mn-O \rangle$
577 distances (1.91-1.92 \AA) and hexagonal symmetry with small b unit-cell dimensions (2.84-
578 2.85 \AA). In contrast, NaBi and KBi₁₀ layers are almost devoid of vacancy and the layer deficit
579 arises essentially from the presence of layer Mn^{3+} cations (25-30%), whose presence induces

580 a higher $\langle \text{Mn-O} \rangle$ distance ($>1.94 \text{ \AA}$). In the latter case Jahn-Teller distorted Mn^{3+} octahedra
581 are ordered at room temperature and their systematic elongation along the **a** axis leads to an
582 orthogonal layer symmetry. When temperature is increased up to 250-350°C, the symmetry of
583 these Mn^{3+} -rich layers becomes hexagonal because of the random orientation of elongated
584 Mn^{3+} octahedra. In this case, $\langle \text{Mn-O} \rangle$ distance remains high ($>1.94 \text{ \AA}$) whereas the *b* unit-
585 cell dimension is increased significantly ($>2.86 \text{ \AA}$). Similar structural features are observed at
586 room temperature when Mn^{3+} octahedra are ordered along the three equivalent directions
587 $[100]$, $[110]$ and $[1\bar{1}0]$ of the **ab** plane, as in lithiophorite.

588 This global multi-parameter relationship between layer cation composition, $\langle \text{Mn-O} \rangle$
589 distances, *b* parameter values and layer symmetry allows deducing fundamental crystal-
590 structure information on the origin of the layer charge and on the location of Mn^{3+} cations,
591 when present (within the octahedral layer or in the interlayer), even for poorly crystallized
592 birnessite varieties. Such inference was recently demonstrated by Villalobos et al. for
593 turbostratic birnessite samples and further discussed by Drits et al. [96,97].

594 **Interlayer Structure of KBi_{10} .** In KBi_{10} , the cohesion between adjacent layers mainly
595 results from the electrostatic interaction between the interlayer K^+ cations and O_{layer} , H-bonds
596 between $\text{H}_2\text{O}_{\text{interlayer}}$ and O_{layer} providing additional ties between layers. K^+ cations occupy one
597 of the three possible sites in the interlayer prisms (Fig. 4). In such position, four $\text{K-O}_{\text{layer}}$
598 distances are shorter than the other two (~ 2.95 and $\sim 3.28 \text{ \AA}$, respectively – Table 4). A similar
599 shift of the interlayer K^+ position was reported for KBi_8 and hydrothermal KBi_{hydr} birnessite
600 varieties as resulting from the strong undersaturation of O_{layer} coordinated to only two Mn^{4+}
601 [67,77]. In KBi_{10} , whose layers are essentially vacancy-free, the presence of $\text{Mn}^{3+}_{\text{layer}}$ is
602 responsible for the undersaturation of O_{layer} . When a O_{layer} is coordinated to three Mn^{4+}
603 octahedra, it ideally receives $0.667 \times 3 = 2$ valence units (v.u.) and is fully saturated. If this
604 O_{layer} is coordinated to two Mn^{4+} and one Mn^{3+} , or to one Mn^{4+} and two Mn^{3+} , it becomes
605 partially undersaturated, ideally receiving only $0.667 \times 2 + 0.500 = 1.833$ v.u. or $0.667 +$

606 $0.500 \times 2 = 1.667$ v.u., respectively. Therefore, a specific distribution of Mn^{4+} and Mn^{3+}
607 cations within adjacent layers (Fig. 7), and the resulting distribution of O_{layer} with various
608 degrees of undersaturation, may account for the shift of the K^+ cations within the interlayer
609 prisms, so as to better achieve local charge compensation of most undersaturated O_{layer} .

610 As found for samples KBi_8 and KBi_{hydr} , $\text{H}_2\text{O}_{\text{interlayer}}$, which are located in the interlayer
611 mid-plane, are slightly shifted in the **ab** plane from the prism's edges defined by O_{layer} from
612 adjacent layers towards the nearest Mn_{layer} (Fig. 4B) [67,77]. However, in KBi_{10} $\text{H}_2\text{O}_{\text{interlayer}}$
613 are shifted only along the **a** axis, refined occupancy of equivalent sites being nil. Resulting
614 $\text{H}_2\text{O}-\text{O}_{\text{layer}}$ distances and $\text{O}_{\text{layer}}-\text{H}_2\text{O}-\text{O}_{\text{layer}}$ angle, equal to 2.77 \AA and 132.9° , respectively
615 (Table 4), are typical for H-bonds.

616 **Layer and Interlayer Structures of Dehydrated Samples KBi_{10} .** When heated up to
617 350°C sample KBi_{10} dehydrates, and the basal spacing is decreased from $\sim 7.05 \text{ \AA}$ to $\sim 6.39 \text{ \AA}$
618 (Table 1) due to the departure of $\text{H}_2\text{O}_{\text{interlayer}}$. Additional structural changes resulting from the
619 heating include layer symmetry increase ($2O$ -to- $2H$ transition) as a result of the loss of
620 cooperative Jahn-Teller effect. Despite the symmetry change and the partial interlayer
621 collapse, position of interlayer K^+ cations is essentially unchanged. Such split of the K^+ site
622 has been reported for hexagonal KBi structures (KBi_8 and KBi_{hydr}), both at room temperature
623 and at 350°C [67,77].

624 For sample Vacuum- KBi_{10} , the cooperative Jahn-Teller effect is preserved as no
625 additional energy is available. Apart from the departure of $\text{H}_2\text{O}_{\text{interlayer}}$ and from the resulting
626 interlayer collapse (from $\sim 7.05 \text{ \AA}$ to $\sim 6.47 \text{ \AA}$), the structure of KBi_{10} and in particular its
627 interlayer structure is maintained. K^+ cations occupy split positions similar to those in KBi_{10} ,
628 the six-fold coordination being provided by the nearest O_{layer} from adjacent layers with only
629 limited migration of K^+ towards the center of the interlayer prism to allow for more
630 appropriate $\text{K}-\text{O}_{\text{layer}}$ distances. This similarity between hydrated and dehydrated interlayer
631 structures of high-temperature KBi varieties thus allows using SAED to study the distribution

632 of interlayer K^+ cations in dehydrated KBi_{10} structure, and extrapolating the obtained results
633 to the hydrated structure. Results from such a study will be reported in the fourth paper of the
634 series devoted to the study of high-temperature KBi varieties [66].

635 **Origin of Sample AfterT- KBi_{10} Structural Heterogeneity.** The main difference
636 between KBi_{10} specimens before and after the thermal treatment is a significant broadening,
637 and weakening, of the $20l$ reflections in sample After- KBi_{10} (Figs. 2 and 3). In addition, the
638 fwhm of $20l$ reflections of sample After- KBi_{10} decreases with increasing l index (solid circles
639 – Fig. 3). These effects are similar to those described for heterogeneous KBi_{10h} birnessite
640 [68]. Gaillot et al. demonstrated that these effects arise from the coexistence in the sample of
641 several populations of particles which all have a $2O$ structure but differ from each other by
642 their unit-cell parameters that are related by eq 3 [68]. Two hypotheses were explored to
643 account for this specific variation of the a and b parameters. First, local fluctuations of the
644 redox conditions during cooling of sample 350- KBi_{10} may have led slightly different Mn^{3+}
645 contents in individual crystals. This hypothesis is incompatible with the observed variation of
646 the a and b unit-cell parameters, the a/b ratio determined for AfterT- KBi_{10} being slightly
647 lower (1.805 Å) than that of KBi_{10} (1.811 Å). If in both specimens layer Mn^{3+} octahedra were
648 systematically elongated along the a axis, the a parameter decrease would then be related with
649 the Mn^{3+} -to- Mn^{4+} oxidation during the thermal treatment. However, at 350°C, reduction
650 rather than oxidation was observed for hydrothermal KBi_{hydr} and pyrolusite (MnO_2)
651 [68,77,98].

652 In the second hypothesis, the unit-cell dimension heterogeneity is related to contrasting
653 orientation distribution of the long Mn^{3+} - O_{layer} bonds with respect to the a axis [77]. The
654 maximum a/b ratio corresponds to KBi_{10} particles in which most Mn^{3+} octahedra are oriented
655 with their long bonds along the a axis whereas in particles with lower a/b ratios the long
656 Mn^{3+} -O bonds of some Mn^{3+} octahedra are oriented at $\pm 120^\circ$ with respect to the a axis. Such
657 different azimuthal orientation distributions of Mn^{3+} octahedra likely originates from the

658 cooling rate of 350-KBi₁₀ which was too fast to allow a complete 2*H*-to-2*O* structure
659 transformation. During this “air quenching” the random orientation of a small fraction of
660 elongated Mn³⁺ octahedra was “frozen” in some KBi₁₀ particles.

661

662 **Acknowledgments.** BL and VAD acknowledge financial support from CNRS-PICS 709
663 program. VAD acknowledges also the Russian Science Foundation and the Environmental
664 Geochemistry Group (LGIT) for financial support. ACG thanks Jean-François Bélar (LdC,
665 Grenoble) for technical assistance with its XND Rietveld refinement program. Martine
666 Lanson and Delphine Tisserand (LGIT, Grenoble) and Céline Boissard (Hydr’ASA, Poitiers)
667 are thanked for chemical and DT-TG analyses, respectively.

REFERENCES

- 668
- 669
- 670 (1) R. Giovanoli, E. Stähli, W. Feitknecht, *Helv. Chim. Acta* 53 (1970) 209.
- 671 (2) R. Giovanoli, E. Stähli, W. Feitknecht, *Helv. Chim. Acta* 53 (1970) 453.
- 672 (3) R.G. Burns, V.M. Burns, *Phil. Trans. Roy. Soc. London A* 286 (1977) 283.
- 673 (4) F.V. Chukhrov, A.I. Gorschkov, E.S. Rudnitskaya, A.V. Sivtsov, *Izv. Akad.*
674 *Nauk Geol.* 9 (1978) 67.
- 675 (5) J.E. Post, D.R. Veblen, *Amer. Mineral.* 75 (1990) 477.
- 676 (6) A. Manceau, A.I. Gorshkov, V.A. Drits, *Amer. Mineral.* 77 (1992) 1133.
- 677 (7) A. Manceau, A.I. Gorshkov, V.A. Drits, *Amer. Mineral.* 77 (1992) 1144.
- 678 (8) B. Lanson, V.A. Drits, Q. Feng, A. Manceau, *Amer. Mineral.* 87 (2002) 1662.
- 679 (9) S.L. Suib, *Curr. Opin. Solid State Mat. Sci.* 3 (1998) 63.
- 680 (10) S. Ching, E.J. Welch, S.M. Hughes, A.B.F. Bahadoor, S.L. Suib, *Chem. Mater.*
681 14 (2002) 1292.
- 682 (11) P. Bezdicka, T. Grygar, B. Klapste, J. Vondrak, *Electrochim. Acta* 45 (1999)
683 913.
- 684 (12) Z.H. Liu, X.J. Yang, K. Ooi, *J. Colloid Interface Sci.* 265 (2003) 115.
- 685 (13) D.J. Jones, E. Wortham, J. Roziere, F. Favier, J.L. Pascal, L. Monconduit, *J.*
686 *Phys. Chem. Solids* 65 (2004) 235.
- 687 (14) E. Wortham, B. Bonnet, D.J. Jones, J. Roziere, G.R. Burns, *J. Mater. Chem.* 14
688 (2004) 121.
- 689 (15) H. Kawaoka, M. Hibino, H. Zhou, I. Honma, *Solid State Ionics* 176 (2005)
690 621.
- 691 (16) M. Nakayama, S. Konishi, H. Tagashira, K. Ogura, *Langmuir* 21 (2005) 354.
- 692 (17) M. Nakayama, H. Tagashira, *Langmuir* 22 (2006) 3864.
- 693 (18) S.T. Wong, C. S., *Inorg. Chem.* 31 (1992) 1165.

- 694 (19) S.T. Wong, C. S., *J. of the Chinese Chemical Society* 40 (1993) 509.
- 695 (20) V. Ramamoorthy, A. Ramasubbu, S. Muthusubramanian, S. Sivasubramanian,
696 *Synthetic Communications* 29 (1999) 21.
- 697 (21) Z.H. Liu, X.H. Tang, C.X. Zhang, Q. Zhou, *Chem. Lett.* 34 (2005) 1312.
- 698 (22) Z.M. Wang, Z. Liu, N. Yamashita, H. Kanoh, K. Ooi, *Langmuir* 18 (2002)
699 1957.
- 700 (23) Z.H. Liu, K. Ooi, H. Kanoh, W.P. Tang, T. Tomida, *Chem. Lett.* (2000) 390.
- 701 (24) Z.H. Liu, K. Ooi, H. Kanoh, W.P. Tang, X.J. Yang, T. Tomida, *Chem. Mater.*
702 13 (2001) 473.
- 703 (25) Y.F. Shen, R.P. Zerger, S.L. Suib, L. McCurdy, D.I. Potter, C.L. O'Young, J.
704 *Chem. Soc., Chem. Commun.* (1992) 1213.
- 705 (26) Y.F. Shen, R.P. Zerger, R.N. DeGuzman, S.L. Suib, L. McCurdy, D.I. Potter,
706 C.L. O'Young, *Science* 260 (1993) 511.
- 707 (27) Y.F. Shen, S.L. Suib, C.L. O'Young, *J. Am. Chem. Soc.* 116 (1994) 11020.
- 708 (28) Y.F. Shen, S.L. Suib, C.L. O'Young, *J. Catal.* 161 (1996) 115.
- 709 (29) Q. Feng, K. Yanagisawa, N. Yamasaki, *Chem. Commun.* (1996) 1607.
- 710 (30) Q. Feng, K. Yanagisawa, N. Yamasaki, *Journal of Porous Materials* 5 (1998)
711 153.
- 712 (31) S.L. Brock, N.G. Duan, Z.R. Tian, O. Giraldo, H. Zhou, S.L. Suib, *Chem.*
713 *Mater.* 10 (1998) 2619.
- 714 (32) Q. Feng, H. Kanoh, K. Ooi, *J. Mater. Chem.* 9 (1999) 319.
- 715 (33) S. Ching, K.S. Krukowska, S.L. Suib, *Inorg. Chim. Acta* 294 (1999) 123.
- 716 (34) Z.H. Liu, K. Ooi, *Chem. Mater.* 15 (2003) 3696.
- 717 (35) Q. Feng, *J. Mater. Sci. Lett.* 22 (2003) 999.
- 718 (36) X.H. Feng, F. Liu, W.F. Tan, X.W. Liu, H.Q. Hu, *Science in China Series D*
719 *Earth Sciences* 47 (2004) 760.

- 720 (37) X.H. Feng, W.F. Tan, F. Liu, J.B. Wang, H.D. Ruan, *Chem. Mater.* 16 (2004)
721 4330.
- 722 (38) F.A. Al Sagheer, M.I. Zaki, *Micropor. Mesopor. Mater.* 67 (2004) 43.
- 723 (39) K.A. Malinger, K. Laubernds, Y.C. Son, S.L. Suib, *Chem. Mater.* 16 (2004)
724 4296.
- 725 (40) X.F. Shen, Y.S. Ding, J. Liu, K. Laubernds, R.P. Zerger, M. Polverejan, Y.C.
726 Son, M. Aindow, S.L. Suib, *Chem. Mater.* 16 (2004) 5327.
- 727 (41) X.F. Shen, Y.S. Ding, J. Liu, J. Cai, K. Laubernds, R.P. Zerger, A. Vasiliev, M.
728 Aindow, S.L. Suib, *Advanced Materials* 17 (2005) 805.
- 729 (42) Z.H. Liu, L.P. Kang, K. Ooi, Y. Makita, Q. Feng, *J. Colloid Interface Sci.* 285
730 (2005) 239.
- 731 (43) L.Z. Wang, Y. Ebina, K. Takada, T. Sasaki, *Chem. Commun.* (2004) 1074.
- 732 (44) E. Paterson, R. Swaffield, L. Clark, *Clay Miner.* 29 (1994) 215.
- 733 (45) P. Le Goff, N. Baffier, S. Bach, J.-P. Pereira-Ramos, *Mat. Res. Bull.* 31 (1996)
734 63.
- 735 (46) V.A. Drits, E.J. Silvester, A.I. Gorshkov, A. Manceau, *Amer. Mineral.* 82
736 (1997) 946.
- 737 (47) E.J. Silvester, A. Manceau, V.A. Drits, *Amer. Mineral.* 82 (1997) 962.
- 738 (48) A. Manceau, B. Lanson, M.L. Schlegel, J.-C. Harge, M. Musso, L. Eybert
739 Berard, J.-L. Hazemann, D. Chateigner, G.M. Lambie, *Amer. J. Sci.* 300 (2000) 289.
- 740 (49) A. Manceau, N. Tamura, R.S. Celestre, A.A. MacDowell, N. Geoffroy, G.
741 Sposito, H.A. Padmore, *Environ. Sci. Technol.* 37 (2003) 75.
- 742 (50) D.C. Golden, J.B. Dixon, C.C. Chen, *Clays & Clay Miner.* 34 (1986) 511.
- 743 (51) R.M. Cornell, R. Giovanoli, *Clays & Clay Miner.* 36 (1988) 249.
- 744 (52) S.H. Kim, W.M. Im, J.K. Hong, S.M. Oh, *J. Electrochem. Soc.* 147 (2000) 413.
- 745 (53) W. Buser, P. Graf, W. Feitknecht, *Helv. Chem. Scripta* 37 (1954) 2322.

- 746 (54) R.M. McKenzie, *Miner. Mag.* 38 (1971) 493.
- 747 (55) H.F. Herbstein, G. Ron, A. Weissman, *J. Chem. Soc. (A)* (1971) 1821.
- 748 (56) S. Ching, J.A. Landrigan, M.L. Jorgensen, N. Duan, S.L. Suib, C.L. O'Young,
749 *Chem. Mater.* 7 (1995) 1604.
- 750 (57) R.J. Chen, P. Zavalij, M.S. Whittingham, *Chem. Mater.* 8 (1996) 1275.
- 751 (58) S.H. Kim, S.J. Kim, S.M. Oh, *Chem. Mater.* 11 (1999) 557.
- 752 (59) Y.U. Jeong, A. Manthiram, *J. Solid State Chem.* 156 (2001) 331.
- 753 (60) K. Kuma, A. Usui, W. Paplawsky, B. Gedulin, G. Arrhenius, *Miner. Mag.* 58
754 (1994) 425.
- 755 (61) Y. Ma, J. Luo, S.L. Suib, *Chem. Mater.* 11 (1999) 1972.
- 756 (62) R.J. Chen, T. Chirayil, P. Zavalij, M.S. Whittingham, *Solid State Ionics* 86-88
757 (1996) 1.
- 758 (63) S. Ching, J.L. Roark, N. Duan, S.L. Suib, *Chem. Mater.* 9 (1997) 750.
- 759 (64) S. Ching, D.J. Petrovay, M.L. Jorgensen, S.L. Suib, *Inorg. Chem.* 36 (1997)
760 883.
- 761 (65) S. Ching, S.L. Suib, *Comment Inorganic Chem.* 19 (1997) 263.
- 762 (66) A.-C. Gaillot, V.A. Drits, B. Lanson, *Micropor. Mesopor. Mater.* (2006) in
763 preparation.
- 764 (67) A.-C. Gaillot, D. Flot, V.A. Drits, A. Manceau, M. Burghammer, B. Lanson,
765 *Chem. Mater.* 15 (2003) 4666.
- 766 (68) A.-C. Gaillot, V.A. Drits, A. Plancon, B. Lanson, *Chem. Mater.* 16 (2004)
767 1890.
- 768 (69) V.A. Drits, *Electron diffraction and high-resolution electron microscopy of*
769 *mineral structures*, Springer Verlag, Berlin Heidelberg, 1987, p 304.
- 770 (70) V.A. Drits, B. Lanson, A.I. Gorshkov, A. Manceau, *Amer. Mineral.* 83 (1998)
771 97.

- 772 (71) V.A. Drits, B. Lanson, C. Bougerol Chaillout, A.I. Gorshkov, A. Manceau,
773 Amer. Mineral. 87 (2002) 1646.
- 774 (72) K.J. Vetter, N. Jaeger, Electrochim. Acta 11 (1966) 401.
- 775 (73) J.J. Lingane, R. Karplus, Ind. Eng. Chem. Anal. Ed. 18 (1946) 191.
- 776 (74) J.-F. Bézar, G. Baldinozzi, CPD Newsletter 20 (1998) 3.
- 777 (75) A.L. Ankudinov, J.J. Rehr, Physical Review B 56 (1997) R1712.
- 778 (76) M.M. Thackeray, A. de Kock, W.I.F. David, Mat. Res. Bull. 28 (1993) 1041.
- 779 (77) A.-C. Gaillot, B. Lanson, V.A. Drits, Chem. Mater. 17 (2005) 2959.
- 780 (78) H.P. Klug, L.E. Alexander, X-ray diffraction procedures for polycrystalline
781 and amorphous materials, Wiley, New York, 1974, p 966.
- 782 (79) B. Lanson, V.A. Drits, A.-C. Gaillot, E. Silvester, A. Plancon, A. Manceau,
783 Amer. Mineral. 87 (2002) 1631.
- 784 (80) B. Lanson, V.A. Drits, E.J. Silvester, A. Manceau, Amer. Mineral. 85 (2000)
785 826.
- 786 (81) M.A. Marcus, A. Manceau, M. Kersten, Geochim. Cosmochim. Acta 68 (2004)
787 3125.
- 788 (82) A. Manceau, M.A. Marcus, N. Tamura, O. Proux, N. Geoffroy, B. Lanson,
789 Geochim. Cosmochim. Acta 68 (2004) 2467.
- 790 (83) A. Manceau, C. Tommaseo, S. Rihs, N. Geoffroy, D. Chateigner, M. Schlegel,
791 D. Tisserand, M.A. Marcus, N. Tamura, Z.S. Chen, Geochim. Cosmochim. Acta 69 (2005)
792 4007.
- 793 (84) A. Manceau, V.A. Drits, E.J. Silvester, C. Bartoli, B. Lanson, Amer. Mineral.
794 82 (1997) 1150.
- 795 (85) J. Töpfer, M. Trari, P. Gravereau, J.P. Chaminade, J.P. Doumerc, Z.
796 Kristallogr. 210 (1995) 184.
- 797 (86) R.D. Shannon, Acta Crystallogr. A32 (1976) 751.

- 798 (87) B.K. Teo, EXAFS: basic principles and data analysis, Springer-Verlag, Berlin,
799 1986, p 349.
- 800 (88) A.L. Foster, G.E. Brown, G.A. Parks, Geochim. Cosmochim. Acta 67 (2003)
801 1937.
- 802 (89) A. Jurgensen, J.R. Widmeyer, R.A. Gordon, L.I. Bendell Young, M.M. Moore,
803 E.D. Crozier, Amer. Mineral. 89 (2004) 1110.
- 804 (90) S.M. Webb, B.M. Tebo, J.R. Bargar, Amer. Mineral. 90 (2005) 1342.
- 805 (91) M. Bellotto, B. Rebours, O. Clause, J. Lynch, D. Bazin, E. Elkaïm, J. Phys.
806 Chem. 100 (1996) 8527.
- 807 (92) T. Ressler, S.L. Brock, J. Wong, S.L. Suib, J. Phys. Chem. B 103 (1999) 6407.
- 808 (93) J.E. Post, D.E. Appleman, Amer. Mineral. 79 (1994) 370.
- 809 (94) R.D. Shannon, P.S. Gumeman, J. Chenavas, Amer. Mineral. 60 (1975) 714.
- 810 (95) F.V. Chukhrov, B.A. Sakharov, A.I. Gorshkov, V.A. Drits, Y.P. Dikov, Int.
811 Geol. Rev. 27 (1985) 1082.
- 812 (96) M. Villalobos, B. Lanson, A. Manceau, B. Toner, G. Sposito, Amer. Mineral.
813 91 (2006) 489.
- 814 (97) V.A. Drits, B. Lanson, A.-C. Gaillot, Amer. Mineral. (2006) submitted.
- 815 (98) Z.L. Wang, J.S. Yin, Y.D. Jiang, Micron 31 (2000) 571.

816

817

Figure captions

818

819 **Fig. 1.** Experimental TG and DT traces obtained for untreated sample KBi_{10} . Analytical
820 conditions are given in the text.

821 **Fig. 2.** Experimental powder XRD patterns obtained for KBi_{10} samples. (A) Pattern recorded
822 at room temperature (KBi_{10}). (B) to (E) Patterns recorded *in situ* at successively
823 100°C, 150°C, 250°C and 350°C (samples 100- KBi_{10} , 150- KBi_{10} , 250- KBi_{10} , 350-

824 KBi₁₀, respectively). (F) Pattern recorded after complete thermal treatment to 350°C
 825 and subsequent cooling to room temperature (sample AfterT-KBi₁₀). (G) Pattern
 826 recorded under vacuum condition (sample Vacuum-KBi₁₀). (H) Pattern recorded
 827 after the sample was brought back to atmospheric pressure (sample AfterVac-
 828 KBi₁₀). Dotted and dot-dashed lines indicate the position of 00*l* reflections for
 829 hydrated and dehydrated samples, respectively. Intensity scale is enlarged over the
 830 30-80° 2θ CuKα angular range, by 9×, 18×, 14×, 13×, 7×, 10×, 14× and 17×, for
 831 XRD pattern shown in (A) to (G), respectively. Reflections are indexed using
 832 orthorhombic *C*-centered 2*O* (A-C, F-G) or 2*H* (D-E) unit cells (see supplementary
 833 material). Super-reflections are indicated by star symbols.

834 **Fig. 3.** Evolution of the full width at half-maximum intensity (fwhm) of 20*l* and 11*l*
 835 reflections (circles and triangles respectively) as a function of the Miller index *l* for
 836 samples KBi₁₀ (open symbols) and AfterT-KBi₁₀ (solid symbols). Experimental
 837 fwhm values are corrected by a cosθ factor to account for crystal-size broadening
 838 [78].

839 **Fig. 4.** Structure model for KBi₁₀. (A) Projection along the **b** axis. Open and solid symbols
 840 indicate atoms at *y* = 0 and *y* = ±1/2, respectively. Large circles represent O_{layer}
 841 atoms, small circles represent Mn_{layer} atoms, shaded circles represent K_{interlayer} and
 842 open circles with dashed outline represent H₂O_{interlayer}. Dot-dashed lines outline the
 843 interlayer prisms defined by two empty tridentate layer cavities. The center of these
 844 prisms is shown by regular dashed lines, and the arrows outline the shift of K⁺
 845 cations from this ideal position. Solid lines represent H-bonds between O_{layer} and
 846 H₂O_{interlayer}, and the arrows outline the shift of H₂O along the **a** axis from the edge
 847 of interlayer prisms. (B) Projection on the **ab** plane. The upper surface of the lower
 848 layer is shown as light shaded triangles. O_{layer} and Mn_{layer} atoms of this lower layer
 849 are shown as small solid and open circles, respectively. Large shaded circles

850 represent interlayer potassium, and open circles with dashed outline represent water
851 molecules. The arrows outline the shift of H₂O along the **a** axis.

852 **Fig. 5.** Comparison between experimental (crosses) and calculated (solid line) XRD patterns
853 for KBi₁₀ samples. (A) Sample KBi₁₀, (B) sample 350-KBi₁₀ and (C) sample
854 Vacuum-KBi₁₀. Atomic coordinates, site occupancies and other structural
855 parameters used for the calculations are listed in Table 3. Difference plot is given
856 for each case. Angular regions with significant contributions from super-reflections
857 were excluded from the fits.

858 **Fig. 6.** k^3 -weighted EXAFS spectra and Fourier transforms (modulus and imaginary parts) of
859 k -weighted EXAFS spectra for KBi₁₀, triclinic 1*T* NaBi and hexagonal 1*H* HBi
860 (pH4). The EXAFS spectrum of KBi₁₀ has the same shape as that of NaBi, but a
861 lower frequency, which manifests itself in a shift to lower distance of the Mn-O and
862 Mn-Mn pairs in the real space.

863 **Fig. 7.** Idealized distribution in projection on the **ab** plane of undersaturated O_{layer} within an
864 interlayer region. 4+ represent Mn⁴⁺ cations located in the lower and/or in the upper
865 octahedral layer. 3+ on black and white backgrounds represent Mn³⁺ cations located
866 in the lower and upper octahedral layers, respectively. Circles represent O_{layer} from
867 both the upper and lower surfaces of adjacent octahedral layers whose positions
868 coincide in projection on the **ab** plane and define the edges of interlayer prisms.
869 Different circle symbols are used to represent the degree of under-saturation of the
870 O-O edge as a function of the total number of Mn³⁺_{layer} coordinated to it (from 0-4 –
871 See figure for equivalence). (A) Mn³⁺-rich rows from adjacent layers coincide in
872 projection on the **ab** plane. (B) Mn³⁺-rich rows from adjacent layers do not coincide
873 in projection on the **ab** plane (shift along the **a** axis).

Table 1: Unit-Cell Parameters of KBi_{10} Samples

	a^a	b	c	a/b	Polytype ^b
KBi_{10}	5.1554(3)	2.8460(1)	14.088(1)	1.811	2O
100- KBi_{10}	5.141(1)	2.850(0)	14.002(2)	1.804	2O
150- KBi_{10}	5.117(1)	2.845(0)	12.860(2)	1.798	2O
150- KBi_{10}	5.010(3)	2.891(1)	12.871(4)	1.733	2H
350- KBi_{10}	5.010(2)	2.894(1)	12.954(7)	1.731	2H
AfterT- KBi_{10}	5.149(3)	2.846(1)	14.042(7)	1.809	2O
Vacuum- KBi_{10}	5.114(2)	2.840(1)	12.787(3)	1.801	2O
AfterVac- KBi_{10}	5.160(2)	2.844(1)	14.072(5)	1.815	2O

^a All parameters are expressed in Å. $\alpha = \beta = \gamma = 90^\circ$. ^b Indexations for 2O and 2H polytypes are given as supplementary material.

Table 2: Crystal data and structure refinement for the KBi₁₀ sample

Ideal formula	$\text{K}^{+}_{0.314}(\text{Mn}^{3+}_{0.246}\text{Mn}^{4+}_{0.737}\square_{0.017})\text{O}_2 \cdot 0.50\text{H}_2\text{O}$
Wavelength	1.54056 Å + 1.54439 Å (Rel. Int. 0.476)
Space group	<i>Ccmm</i>
Unit-cell dimensions	$a = 5.1554(3)$ Å
	$b = 2.8460(1)$ Å
	$c = 14.088(1)$ Å
	$V = 206.70$ Å ³
Angular range	34-90°
Data / Parameters	1319 / 13
Number of reflections	100
R _{Exp}	3.5%
R _{wp}	11.21%
R _{Bragg}	5.55%
Goodness of fit	3.16

Table 3. Atomic Positions and Site Occupancies for $\text{KBi}_{10} 2O$, Vacuum- $\text{KBi}_{10} 2O$ and 350- $\text{KBi}_{10} 2H$ Samples

	KBi₁₀				Vacuum-KBi₁₀				350-KBi₁₀			
	x^a	y	z	Occ.	x	y	z	Occ.	x	y	z	Occ.
Mn _{layer}	0	0	0	0.985(6)	0	0	0	0.983	0	0	0	0.983
O _{layer}	0.342(1)	0	0.0700(6)	2.000	0.341	0	0.0762	2.000	0.333	0	0.0788	2.000
K	-0.253(24)	0	1/4	0.077(28)	-0.300	0	1/4	0.121	-0.300	0	1/4	0.104
K	0.134(8)	±0.375(23))	1/4	0.235(28)	0.153	±0.459	1/4	0.191	0.150	±0.450	1/4	0.208
H ₂ O	0.127(5)	0	1/4	0.500								

^a Atomic positions are given according to orthogonal axes, even for *2H* 350- KBi_{10} . The values of Debye-Waller factors (B) are 0.5, 1.0, 2.0, 2.0 for Mn_{layer}, O_{layer}, K and H₂O, respectively.

Table 4. Selected Inter-Atomic Distances in High-Temperature KBi₁₀ Samples

	KBi₁₀	Vacuum-KBi₁₀	350-KBi₁₀
Height of Mn layer	1.972 ^a	1.974	2.015
Mn _{layer} -Mn _{layer}	short	2.846(0) × 2	2.839 × 2
	long	2.944(0) × 4	2.924 × 4
	average	2.911	2.896
Mn _{layer} -O _{layer}	short	1.914(5) × 4	1.903 × 4
	long	2.018(6) × 2	1.998 × 2
	average	1.949	1.934
K-O _{layer}	short	2.948(28)-2.973(23) × 4	2.735 × 4
	long	3.277(78)-3.287(38) × 2	2.868 × 2
	average	3.061-3.067	2.784
K _{interlayer} -H ₂ O _{interlayer}	3.197(137) - 3.611(49)		
O _{layer} -H ₂ O _{interlayer}	2.767(12)		
O _{layer} -H ₂ O-O _{layer} angle	132.88(25) ^o		

^a All distances in Å.

Table 5. EXAFS Parameters for the Nearest Mn-O and Mn-Mn Pairs in Birnessite Samples and in the Reference λ -MnO₂

Sample	$R+\Delta R$ window (Å)	fit interval (Å ⁻¹)	shell	R^a (Å)	CN ^b	σ_c^2 (Å ²)	ΔE^d (eV)	residual ^e
λ -MnO ₂	1.1 - 3.3	$3.7 < k < 13.5$	Mn-O	1.91	6	25×10^{-4}	1.5	12
			Mn-Mn _{edge}	2.85	6	28×10^{-4}		
			Mn-O ^f	3.52	6 ^g	88×10^{-4}		
HBi ^h	1.1 - 3.4	$3.7 < k < 12$	Mn-O	1.91	4.5	32×10^{-4}	1.6	7
			Mn-Mn _{edge}	2.89	4.8	$51 \times 10^{-4 i}$		
			Mn-Mn _{corner}	3.49	2.8	$51 \times 10^{-4 i}$		
			Mn-O ^f	3.61	6 ^g	49×10^{-4}		
NaBi ^h	1.1 - 3.7	$3.7 < k < 13.5$	Mn-O	1.92	5.6	30×10^{-4}	0.7	14
			Mn-Mn _{edge}	2.89	3.6	$40 \times 10^{-4 i}$		
			Mn-Mn _{edge}	3.01	2.4	$40 \times 10^{-4 i}$		
			Mn-O ^f	3.57	6 ^g	12×10^{-3}		
KBi ₁₀	1.1 - 3.7	$3.7 < k < 12$	Mn-O	1.91	4.8	29×10^{-4}	1.3	14
			Mn-Mn _{edge}	2.89	3.5	$29 \times 10^{-4 i}$		
			Mn-Mn _{edge}	3.02	1.6	$29 \times 10^{-4 i}$		
			Mn-O ^f	3.58	6 ^g	14×10^{-3}		

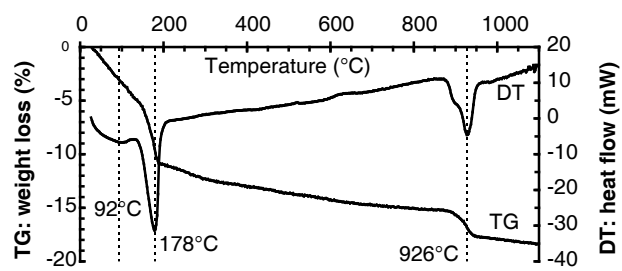
^a Accuracy and precision in average distances are ± 0.02 and ± 0.01 Å, respectively. In λ -MnO₂, the crystallographic Mn-O and Mn-Mn distances are 1.91 Å and 2.84 Å, respectively [76]. ^b Coordination number. The scaling factor S_0^2 was calculated to obtain CN = 6 in the reference λ -MnO₂: $S_0^2 = 0.73$ for the Mn-O pair and 0.80 for the Mn-Mn pair [96]. Typical accuracy on coordination numbers is ± 1.5 . ^c Debye-Waller factor. ^d Variation of the energy threshold treated as a single adjustable parameter for all subshells. ^e Residual is calculated from $R = [\sum|(k^3\chi_{\text{exp}} - k^3\chi_{\text{cal}})| / \sum k^3\chi_{\text{exp}}] \times 100$. ^f Second Mn-O shell. ^g Fixed value in the optimization procedure. ^h EXAFS results are, within accuracy, identical to those published by Silvester et al. [47]. ⁱ Parameter varied but constrained equal for the two subshells.

Table 6. EXAFS Parameters for the Nearest Mn-O and Mn-Mn Pairs in Birnessite Reported by Webb et al. [90]

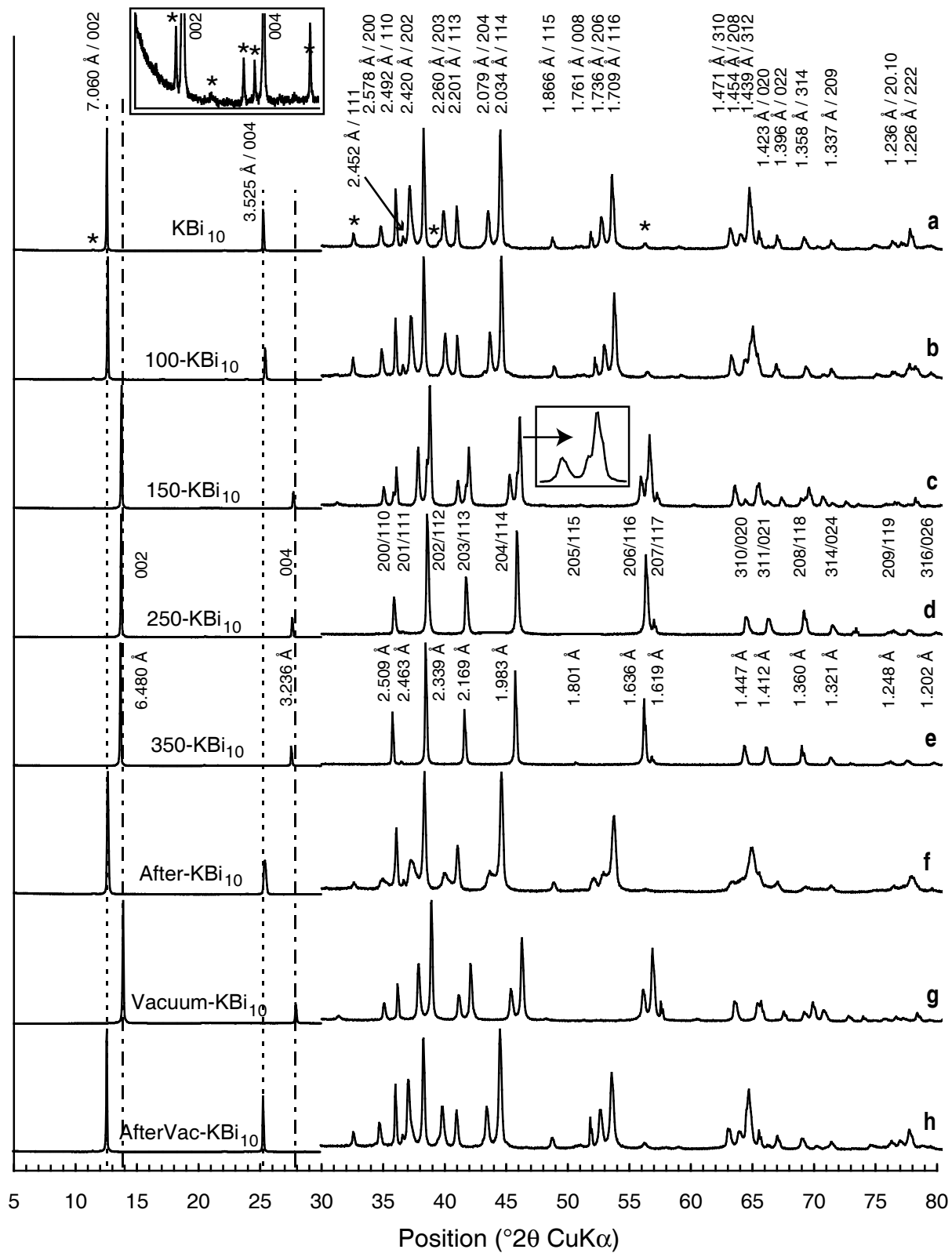
Sample	shell	XRD ^a		EXAFS		
		<i>R</i> (Å)	<i>CN</i> ^b	<i>R</i> (Å)	<i>CN</i>	σ_r^2 (Å ²)
NaBi	Mn-O	1.92	2	1.87 (2)	4 ^b	0.005 (2)
		1.94	2	1.94 (1)	2 ^b	0.002 (1)
		2.00	2			
	Mn-Mn _{edge}	2.85	2	2.88 (3)	2 ^c	0.006 (1) ^d
		2.95	4	2.90 (3)	4 ^c	0.006 (1) ^d
	Mn-Mn _{corner}	-	-	3.36 (9)	0.8 (8)	0.006 (3)
HBi	Mn _{layer} -O	1.92	5	1.89 (3)	4 ^c	0.008 (2)
	Mn _{interlayer} -O	1.98	0.5	1.90 (2)	2 ^c	0.004 (2)
	Mn-H ₂ O	2.08	0.5			
	Mn-Mn _{edge}	2.85	3.5	2.84 (1)	2 ^c	0.005 (1) ^d
				2.89 (1)	4 ^c	0.005 (1) ^d
	Mn-Mn _{corner}	3.54	1.8	3.48 (1)	2.0 (1.1)	0.003 (3)

^aData from Lanson et al. [8,80]. ^bTheoretical EXAFS CN values calculated from XRD data. ^c

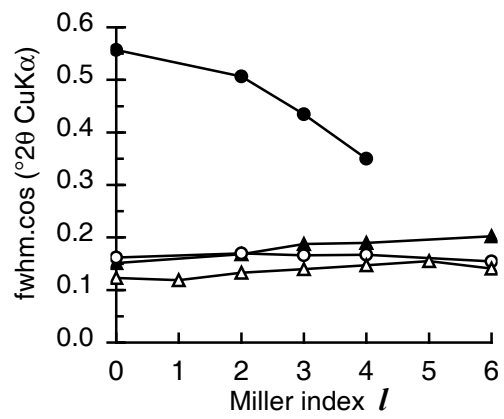
CN values were fixed during the fit. ^dParameter varied but constrained equal for the two subshells.



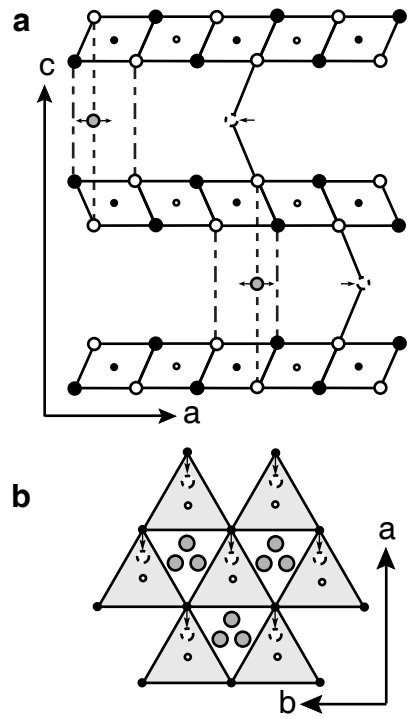
Please print in one column format



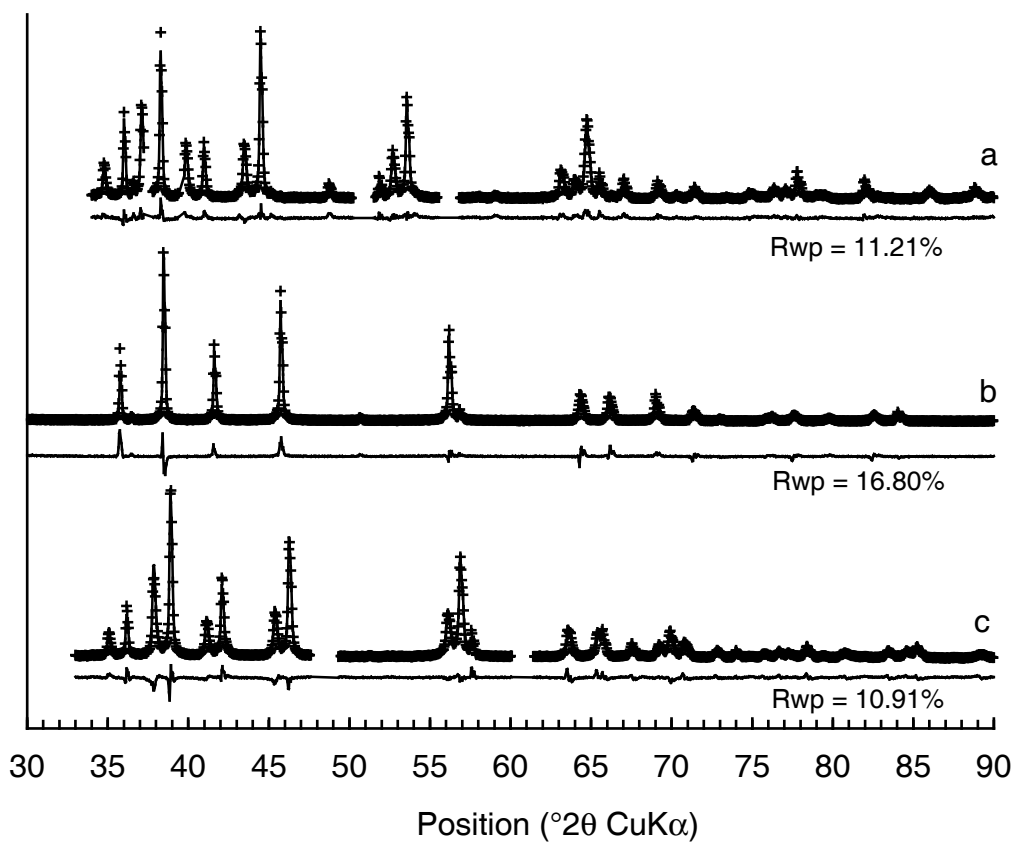
Please print in two column format



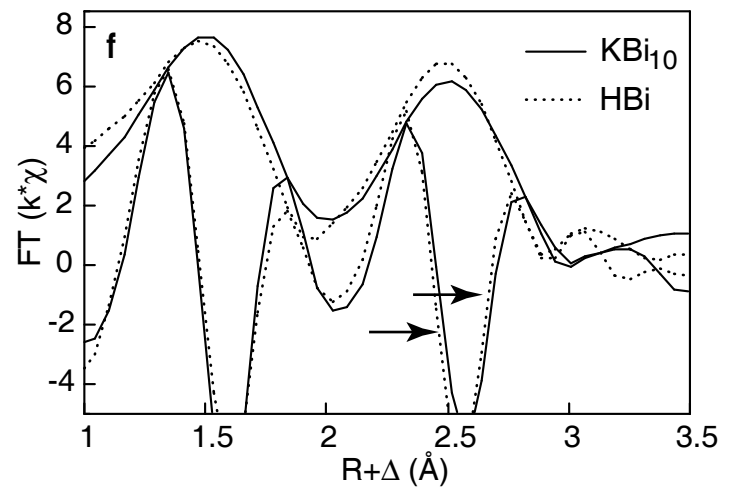
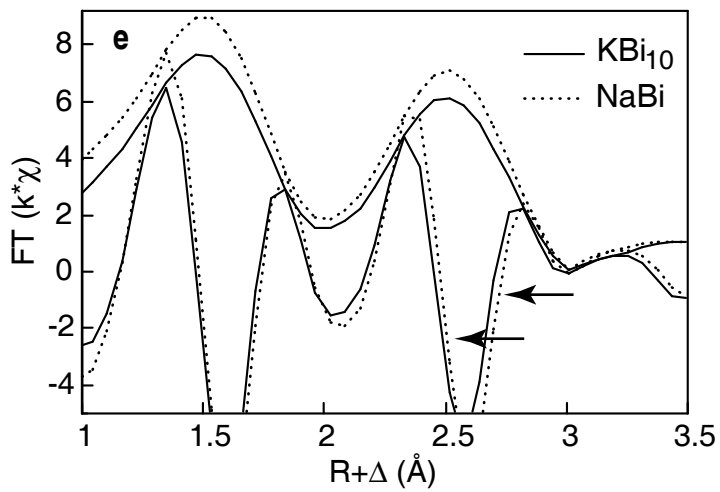
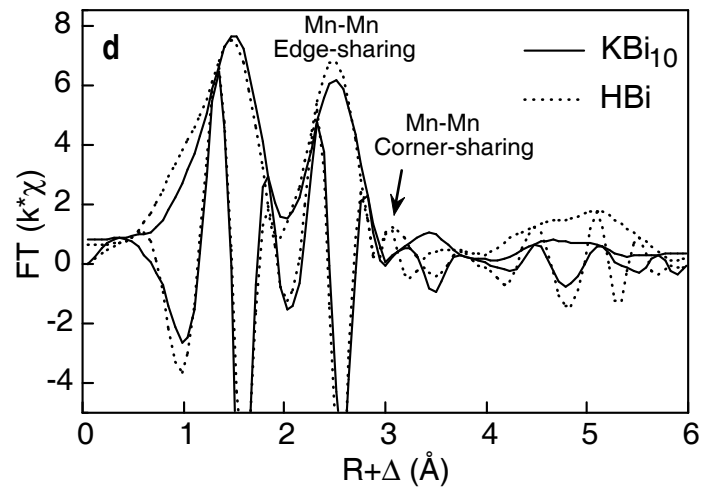
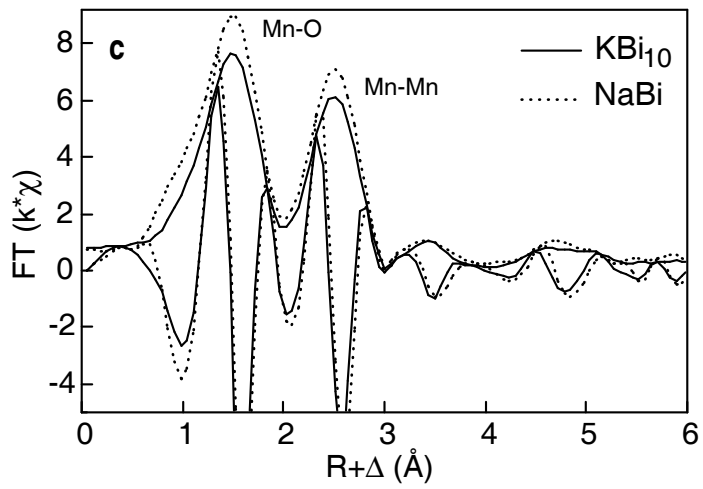
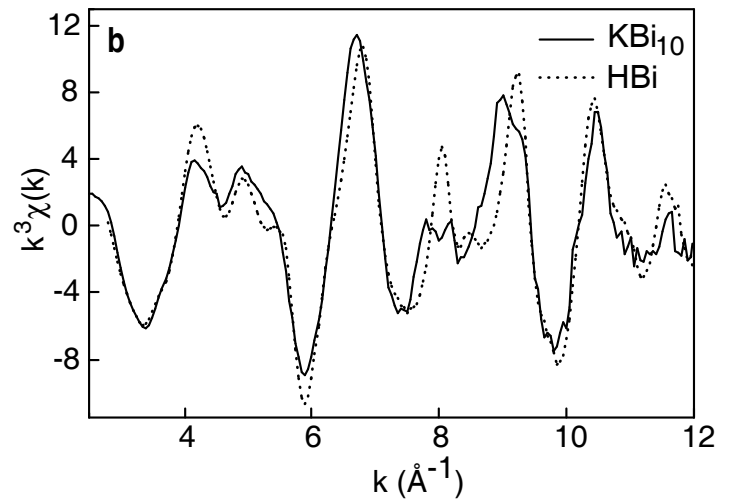
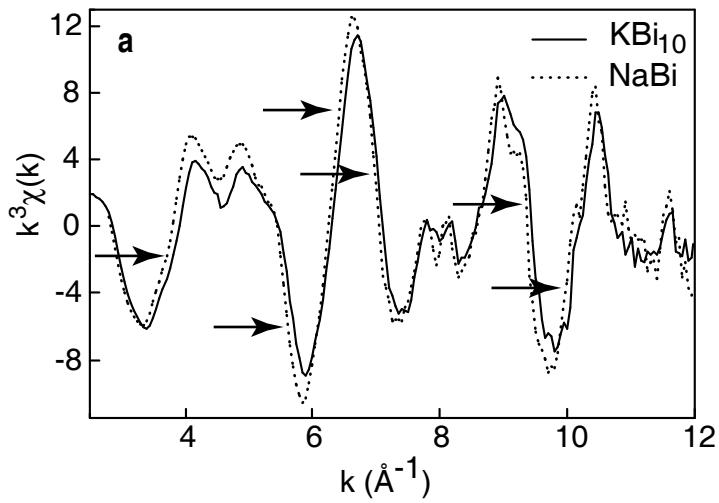
Please print in one column format



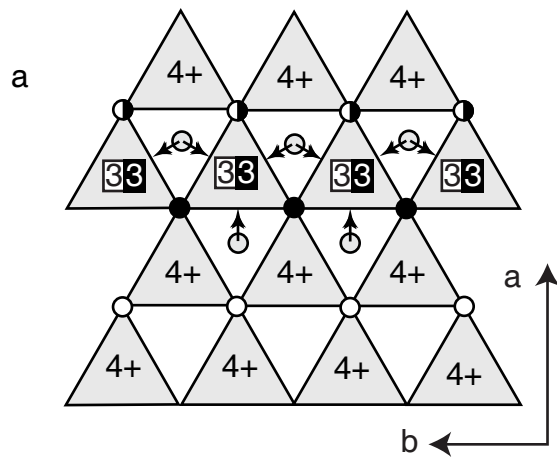
Please print in one column format



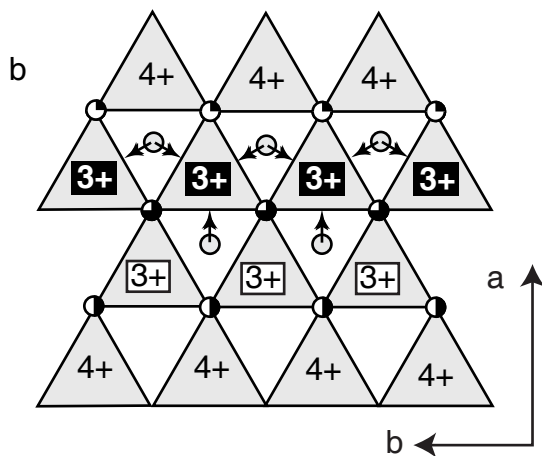
Please print in two column format



Please print in two column format



○ 0 ● 1 ● 2 ● 3 ● 4
 33 layers 1 and 2
 3+ layer 1 3+ layer 2



Please print in one column format

Indexing in Terms of the 2O Polytype of the Experimental XRD Patterns of KBi₁₀, AfterT-KBi₁₀, Vacuum-KBi₁₀, 100-KBi₁₀, and 150-KBi₁₀ (Main Phase).

2O	KBi ₁₀		AfterT-KBi ₁₀		Vacuum-KBi ₁₀		100-KBi ₁₀		150-KBi ₁₀	
<i>hkl</i>	<i>d</i> _{exp} ^a	<i>d</i> _{calc} ^b	<i>d</i> _{exp}	<i>d</i> _{calc}	<i>d</i> _{exp}	<i>d</i> _{calc}	<i>d</i> _{exp}	<i>d</i> _{calc}	<i>d</i> _{exp}	<i>d</i> _{calc}
	7.750 ^c	7.733	7.691		7.653		7.722		7.706	
002 ^d					6.944					
002	7.060	7.050	7.021	7.022	6.394	6.390	6.995	7.000	6.435	6.430
	6.784	6.780					5.191			
	5.206	5.210			4.375		3.998		4.385	
	4.013	4.016	4.006		4.257		3.866		4.260	
	3.730	3.729	3.719		3.723		3.718		3.754	
004					3.486					
004	3.525	3.525	3.506	3.511	3.195	3.195	3.501	3.500	3.216	3.215
	3.202	3.207			3.111		3.193			
	2.745	2.745	2.744		2.850		2.748		2.857	
200	2.578	2.578	2.572	2.569	2.557	2.556	2.572	2.571	2.559	2.559
110	2.492	2.492	2.488	2.489	2.483	2.481	2.494	2.493	2.488	2.487
111	2.452	2.454		2.451		2.436	2.455	2.455		2.442
202	2.420	2.421	2.414	2.412	2.375	2.373	2.413	2.413	2.377	2.377
	2.403	2.405								
112	2.348	2.349	2.345	2.346	2.313	2.313	2.348	2.349	2.319	2.320
006		2.349		2.341		2.130		2.333		2.144
	2.276	2.278								
203	2.260	2.260	2.255	2.252	2.192	2.192	2.252	2.252	2.197	2.197
113	2.201	2.201	2.198	2.198	2.144	2.144	2.199	2.199	2.152	2.151
							2.091			
204	2.079	2.081	2.071	2.073	1.997	1.996	2.072	2.072	2.003	2.002
114	2.034	2.035	2.030	2.031	1.961	1.960	2.030	2.036	1.967	1.967
							2.007			1.814
205				1.895		1.807		1.894		
115	1.866	1.867	1.864	1.863		1.780	1.862	1.862	1.787	1.788
008	1.761	1.763	1.758	1.755	1.599	1.598	1.751	1.750	1.608	1.609
							1.797			
206	1.736	1.737	1.731	1.730	1.637	1.636	1.728	1.728	1.643	1.643
116	1.709	1.710	1.705	1.705	1.617	1.616	1.704	1.704	1.624	1.624
					1.553		1.691		1.536	
	1.634		1.632		1.528		1.630		1.501	
					1.504		1.560			
					1.487					
310	1.471	1.471	1.467	1.467	1.462	1.461	1.469	1.469	1.463	1.463
208	1.454	1.455	1.451	1.449	1.356	1.355	1.447	1.447	1.361	1.361
118	1.439	1.439	1.436	1.435	1.345	1.343	1.433	1.432	1.350	1.350
312	1.439	1.439	1.436	1.436	1.425	1.424	1.437	1.437	1.426	1.427
020	1.423	1.423	1.423	1.423	1.421	1.419	1.426	1.426		1.423
022	1.396	1.395	1.395	1.395	1.387	1.385	1.396	1.397	1.389	1.389
							1.387		1.380	
314	1.358	1.358	1.356	1.354	1.330	1.329	1.354	1.354	1.331	1.332
209	1.337	1.339	1.334	1.334			1.331	1.331		
024	1.319	1.320	1.320	1.319	1.298	1.297	1.320	1.320	1.301	1.301
119	1.319	1.302	1.320	1.322			1.320	1.320		
00.10				1.404		1.278		1.400	1.286	1.286
400				1.284	1.279	1.278		1.285		1.280
					1.267					
					1.260					
402				1.263	1.254	1.253	1.264	1.264	1.256	1.255
					1.249					
220	1.246	1.246	1.245	1.245	1.242	1.241	1.246	1.247	1.243	1.244

316			1.245	1.243			1.246	1.243	1.209	1.208
20.10	1.236	1.237		1.232				1.229	1.149	1.149
222	1.226	1.227	1.226	1.226	1.219	1.218	1.227	1.227	1.221	1.221
11.10	1.226	1.227	1.226	1.223	1.136	1.136	1.221	1.221	1.142	1.142
	<i>1.209</i>						<i>1.239</i>			
223			1.204	1.203		1.193	1.205	1.204	1.194	1.194
404			1.204	1.206		1.187	1.205	1.206	1.188	1.189
224	1.175	1.175	1.173	1.173	1.157	1.157	1.174	1.174	1.160	1.160
00.12			1.173	1.173			1.167	1.167		
							<i>1.160</i>			
					1.131		<i>1.155</i>			
405			1.169	1.168	1.145	1.143				
11.11				1.136			1.133	1.134		
225			1.130	1.138		1.116	1.133	1.139		
318				1.126		1.078	1.125	1.125		
406				1.126			1.125	1.126	1.098	1.098
226				1.099			1.099	1.100		

^a $d_{\text{exp}}(hkl)$ are measured experimentally. ^b $d_{\text{calc}}(hkl)$ values are calculated using the unit-cell parameters listed in Table 1. ^c $d(hkl)$ values in italics correspond to super-reflections (see companion article). ^d 002 and 004 reflections from remnant hydrated crystals.

Indexing in Terms of $2H$ Polytypes of the Experimental XRD Patterns of 150-KBi₁₀
(Accessory Phase) and 350-KBi₁₀.

$2H$	150-KBi ₁₀		350-KBi ₁₀	
hkl	d_{exp}^a	d_{calc}^b	d_{exp}	d_{calc}
002	6.435	6.441	6.480	6.489
	<i>4.385^c</i>		<i>4.341</i>	
	<i>4.260</i>		<i>4.130</i>	
	<i>3.754</i>			
004	3.216	3.221	3.236	3.245
200/110	2.502	2.505	2.509	2.510
201/111	2.488	2.459	2.463	2.464
202/112	2.335	2.335	2.339	2.341
203/113	2.163	2.164	2.169	2.171
204/114	<i>1.978</i>	1.978	1.983	1.985
205/115		<i>1.796</i>	1.801	1.804
206/116	1.630	<i>1.630</i>	1.636	1.639
008	1.608	1.610	1.619	1.622
310/020	1.445	<i>1.446</i>	1.447	1.450
312/022	1.410	1.411	1.412	1.415
208/118	1.354	1.355	1.360	1.362
314/024	1.319	1.319	1.321	1.323
00.10	1.286	1.288	1.295	1.298
400/220	1.243	1.253	1.253	1.255
209/119	1.243	1.243	1.248	1.250
402/222	1.229	1.230		1.232
316/026	1.209	1.200	1.202	1.204
404/224	1.167	1.168	1.168	1.171
20.10/11.10	1.149	1.146	1.151	1.153
406/226	1.098	1.083		1.086

^a $d_{\text{exp}}(hkl)$ are measured experimentally. ^b $d_{\text{calc}}(hkl)$ values are calculated using the unit-cell parameters listed in Table 1. ^c $d(hkl)$ values in italics correspond to super-reflections (see companion article).¹

1. A.-C. Gaillot, V. A. Drits and B. Lanson, in preparation.